Defect-mediated snaking: A new growth mechanism for localized structures

Y.-P. Ma [a], J. Burke [b,*], E. Knobloch [a]

[a] Department of Physics, University of California, Berkeley, CA 94720, USA
[b] Department of Mathematics and Statistics, Boston University, Boston, MA 02215, USA

ARTICLE INFO

ABSTRACT

Stationary spatially localized patterns in parametrically driven systems are studied, focusing on the 2:1 and 1:1 resonance tongues as described by the forced complex Ginzburg–Landau equation. Homoclinic snaking is identified in both cases and the nature of the growth of the localized structures along the snaking branches is described. The structures grow from a central defect that inserts new rolls on either side, while pushing existing rolls outwards. This growth mechanism differs fundamentally from that found in other systems exhibiting homoclinic snaking in which new rolls are added at the fronts that connect the structure to the background homogeneous state.

1. Introduction

Spatially localized structures in one spatial dimension correspond to homoclinic orbits of the governing equations written as a dynamical system in space. When this system is *reversible* in space these structures may be reflection-symmetric and hence stationary. Equilibrium structures of this type have been extensively studied in recent years both theoretically [1,2] and numerically [3,4], and are found in bistable regimes, i.e., in parameter regimes with two coexisting equilibria, A and B, say. Two cases are of particular interest: (i) A and B are both spatially homogeneous, (ii) A is spatially homogeneous while B is spatially periodic. The associated localized structures are organized by heteroclinic *cycles*, i.e., connections of the form $A \to B \to A$ or vice versa. Since the return connection is guaranteed by the reversibility of the vector field a heteroclinic cycle between two homogeneous equilibria in four dimensions is of codimension one while a heteroclinic cycle between a homogeneous and a periodic equilibrium is of codimension zero. In the former case the cycle exists at a particular parameter value; in the latter there is an interval in parameter space filled with such cycles.

The detailed behavior near such cycles depends on the spatial eigenvalues of the homogeneous states and the spatial Floquet multipliers of the periodic states. If the eigenvalues of both homogeneous states are real the fronts connecting state A to state B and back again will be monotonic and a single localized state is present whose length diverges as the heteroclinic cycle is approached. If the eigenvalues of one of the states involved are complex, the fronts will no longer be monotonic, and there will be a finite multiplicity of localized states on either side of the parameter value corresponding to the formation of the heteroclinic cycle. We refer to this behavior as *collapsed snaking* to distinguish it from *homoclinic snaking* that accompanies heteroclinic cycles between homogeneous and periodic equilibria. In this case, localized structures are found in an interval of parameter values that define the so-called snaking [2] or pinning [5] region. This type of behavior is well understood in the context of variational systems such as the Swift–Hohenberg equation [6,7,1]. This equation possesses a trivial homogeneous state and the localized structures bifurcate from this state simultaneously with the branch of spatially periodic states, provided these bifurcate subcritically. At small amplitude the localized structures are broad but as the branch enters the pinning region their width and amplitude become comparable to the wavelength and amplitude of the competing periodic pattern. As one continues to follow localized states towards larger amplitude one finds that the structure broadens by nucleating additional rolls symmetrically on either side. Structures of this type therefore grow from the outside. Associated with this growth are back-and-forth oscillations of the solution branch across the pinning region [7,8]. Generically there are two types of reflection-symmetric localized states, distinguished by having maxima or minima at the point of symmetry. In addition, asymmetric localized states are also present, and in variational systems these also correspond to steady solutions. Such states connect

the two branches of symmetric localized states in a characteristic snakes-and-ladders structure [1]. In addition, the snaking or pinning region contains a multitude of multipulse states, i.e., bound states of localized structures. These may fall on additional snaking branches or be organized in stacks of isolas [9].

In variational systems such as the Swift–Hohenberg equation the origin of this remarkably complex structure can be related to the presence of a Maxwell point at which the homogeneous and periodic equilibria have the same energy. In this case the periodic pattern within the localized structure pins the fronts at either end that connect it to the homogeneous state preventing their motion even when the energies differ [5]. The rich structure of the resulting pinning region is a direct consequence of this effect and may be thought of as the result of a broadening of the Maxwell point owing to the heterogeneity of one of the competing equilibria.

In the systems studied thus far the wavelength of the periodic state within the localized structure appears to be well-defined and is found to be a monotonic function of the bifurcation parameter. In variational systems this behavior is easy to understand using energy considerations [1]. However, a quantitative understanding of the wavelength selection mechanism is only possible in the presence of a Hamiltonian that is conserved by the time-independent system written as a dynamical system in *space* [6].

Recent work by Beck et al. [10] shows that the snakes-and-ladders structure of the pinning region persists when nonvariational terms are added, although the asymmetric ladder states now correspond to *drifting* localized structures [11]. Studies of natural doubly-diffusive convection [12,4] and of binary fluid convection [3] confirm this expectation. These results, taken together, give the impression that all localized structures in a snaking or pinning region grow qualitatively as described by the Swift–Hohenberg equation. We show in this paper that this is not the case. Specifically, we exhibit two examples where the localized structures grow by roll insertion in the center of the structure, accompanied by outward displacement of the existing rolls. The center corresponds to a defect that is responsible for the "cell division" required to grow the structure. The central defect thus plays the role of a steady state "pacemaker".

This new growth mechanism has been discovered in the forced complex Ginzburg–Landau equation describing parametrically driven dissipative media in an appropriate parameter regime [13, 14]. Recent experimental studies of systems driven by spatially homogeneous periodic forcing with frequency near twice the natural oscillation frequency of the system have revealed the presence of different types of localized states, including *oscillons* [15–18] and *reciprocal oscillons* [19–21]. The former are localized time-dependent oscillations that are embedded in a stationary background and oscillate with half the forcing frequency [16,18]. The latter are localized oscillations embedded in an oscillating background, both of which oscillate at half the forcing frequency and out of phase. Bound states of oscillons have also been observed. Spatially localized oscillations are also found in systems driven additively near their natural oscillation frequency [22–24]. In the following we refer to these two cases as 2:1 and 1:1 resonances, respectively.

This paper is organized as follows. In Section 2 we introduce the forced complex Ginzburg–Landau equation used to describe near-resonant forcing of oscillatory systems and summarize the key properties of this equation. In Section 3 we analyze in detail the new types of behavior present in the 2:1 resonance, and in Section 4 we extend our approach to the more difficult 1:1 resonance. These sections rely heavily on numerical continuation using the software AUTO [25]. In Section 5 we describe the results of time integration to examine both the stability of the localized structures we identify and their evolution when they prove to be unstable. The paper concludes with brief remarks in Section 6.

2. The forced complex Ginzburg–Landau equation

We consider a continuous system in one spatial dimension near a bifurcation to spatially homogeneous oscillations with natural frequency ω in the presence of spatially homogeneous forcing with frequency Ω. We focus on the behavior near strong resonances of the form $\Omega{:}\omega = n{:}1$, where $n = 1, 2$. In both cases the forcing leads to an Arnol'd tongue containing spatially homogeneous states that are phase-locked to the forcing frequency Ω. When $n = 1$ the amplitude of the phase-locked states may take the form of an S-shaped curve as the forcing increases, leading to a region with multiple coexisting phase-locked states. Likewise, when $n = 2$ the phase-locked states may bifurcate subcritically on one side of the Arnol'd tongue, again leading to bistability, this time between the trivial background state and a pair of finite amplitude phase-locked states that are 180° out of phase.

In the present paper we suppose that a dynamical observable $w(x, t)$ takes the form

$$w = w_0 + A e^{i\Omega t/n} + c.c. + \cdots, \tag{1}$$

where w_0 represents the homogeneous equilibrium state, $A(x, t)$ is a complex amplitude, and the ellipses denote higher order terms. Under appropriate conditions [13,14] the oscillation amplitude $A(x, t)$ obeys the forced complex Ginzburg–Landau equation (FCGLE)

$$A_t = (\mu + i\nu)A - (1 + i\beta)|A|^2 A + (1 + i\alpha)A_{xx} + \gamma \bar{A}^{n-1}, \tag{2}$$

where μ represents the distance from onset of the oscillatory instability, ν is the detuning from the unforced frequency, and α, β and $\gamma > 0$ represent dispersion, nonlinear frequency correction and the forcing amplitude, respectively. We distinguish two regimes, the regime $\mu < 0$ in which spatially homogeneous oscillations decay in the absence of forcing and $\mu > 0$ in which they grow. We refer to the former as the damped regime and the latter as the self-exciting regime. For numerical exploration it will be useful to write Eq. (2) in terms of real amplitudes $U(x, t)$, $V(x, t)$ such that $A \equiv U + iV$, $\bar{A} \equiv U - iV$.

Eq. (2) is the basic equation studied in this paper. This equation has a large variety of nontrivial solutions, both homogeneous in space and spatially inhomogeneous, for all values of $n \geq 1$; when $n > 1$ it also possesses the trivial solution $A = 0$. These solutions either respect or break the two symmetries of Eq. (2), equivariance under $(x, A) \rightarrow (x, A e^{2\pi i/n})$, and reversibility in space: $(x, A) \rightarrow (-x, A)$. Of interest in the following are localized structures corresponding to solutions that are homoclinic to the same homogeneous state as $|x| \rightarrow \infty$ and fronts corresponding to heteroclinic solutions connecting two distinct spatially homogeneous states. In addition, there are connections between homogeneous states and spatially periodic states created in Turing bifurcations. Finally, we are also interested in homoclinic orbits connecting a periodic orbit to itself. The presence of reversibility renders certain of these connections structurally stable, as discussed further below.

Eq. (2) possesses nontrivial stationary spatially homogeneous solutions of the form $A = R \exp i\phi$, where

$$(1 + \beta^2)R^4 - 2R^2(\mu + \nu\beta) + \mu^2 + \nu^2 = \gamma^2 R^{2n-4} \tag{3}$$

and ϕ solves

$$\sin n\phi = \frac{\nu - \beta R^2}{\gamma R^{n-2}}, \qquad \cos n\phi = \frac{R^2 - \mu}{\gamma R^{n-2}}. \tag{4}$$

For each positive solution of Eq. (3) these equations have n solutions ϕ in $[0, 2\pi)$. This is a consequence of the equivariance of Eq. (2) under $(x, A) \rightarrow (x, A e^{2\pi i/n})$. The temporal stability of these solutions with respect to spatially homogeneous perturbations is determined by writing $A = R \exp(i\phi)(1 + a(t))$, linearizing in $a(t)$,

and looking for solutions of the form $a(t) = a_+ \exp st + \bar{a}_- \exp \bar{s}t$. The (complex) growth rate s obeys the quadratic equation

$$s^2 + 2[R^2 + \gamma R^{n-2} \cos n\phi]s + 2n\gamma R^n (\cos n\phi - \beta \sin n\phi)$$
$$- n(n-2)\gamma^2 R^{2n-4} = 0. \tag{5}$$

This growth rate vanishes at

$$\cos n\phi - \beta \sin n\phi - \frac{1}{2}(n-2)\gamma R^{n-4} = 0, \tag{6}$$

i.e., at saddle–nodes. This equation is equivalent to

$$(1 + \beta^2)R^2 = \mu + \beta\nu + \frac{1}{2}(n-2)\gamma^2 R^{2n-6}. \tag{7}$$

These results hold for all integers $n \geq 1$. A similar calculation shows that the growth rate of perturbations with wavenumber k satisfies the equation

$$s^2 + 2[R^2 + \gamma R^{n-2} \cos n\phi + k^2]s + 2n\gamma R^n (\cos n\phi - \beta \sin n\phi)$$
$$- n(n-2)\gamma^2 R^{2n-4} + 2[(1+\alpha\beta)R^2 + \gamma R^{n-2}$$
$$\times (\cos n\phi - \alpha \sin n\phi)]k^2 + (1+\alpha^2)k^4 = 0, \tag{8}$$

or equivalently

$$s^2 - 2[\mu - k^2 - 2R^2]s + (1+\alpha^2)k^4$$
$$+ 2[2(1+\alpha\beta)R^2 - \mu - \alpha\nu]k^2 - 2nR^2[\mu + \beta\nu$$
$$- (1+\beta^2)R^2] - n(n-2)\gamma^2 R^{2n-4} = 0. \tag{9}$$

A Turing bifurcation occurs at the extremum of the neutral stability curve $s = 0$ in the (k, γ) plane. At this point $\gamma = \gamma^T$, $R = R_T$ and the solution $k = k_T$ has multiplicity two. Thus

$$[2(1+\alpha\beta)R_T^2 - \mu - \alpha\nu]^2 = -n(1+\alpha^2)R_T^2[2(\mu + \beta\nu)$$
$$- 2(1+\beta^2)R_T^2 + (n-2)(\gamma^T)^2 R_T^{2n-6}]. \tag{10}$$

The corresponding Turing wavenumber is given by

$$k_T^2 = \frac{\mu + \alpha\nu - 2(1+\alpha\beta)R_T^2}{1+\alpha^2}. \tag{11}$$

Eq. (10) is to be solved simultaneously with Eq. (3) for the strength γ^T of the forcing at which this bifurcation sets in. The corresponding amplitude R_T then determines the wavelength $2\pi/k_T$ of the resulting structure via Eq. (11). In both cases Hopf bifurcations may arise but these lead to temporally periodic states not considered here.

In the following we study steady spatially localized structures that approach a homogeneous state as $x \to -\infty$ or $x \to +\infty$ or both. Necessary conditions for exponential approach to or departure from such a state are provided by the *spatial* eigenvalues of these states. These are obtained by writing $A = R \exp(i\phi)(1 + a(x))$, linearizing in $a(x)$, and looking for solutions of the form $a(x) = a_+ \exp \lambda x + \bar{a}_- \exp \bar{\lambda}x$. The spatial eigenvalues λ obey the quadratic equation

$$(1+\alpha^2)\lambda^4 - 2[(1+\alpha\beta)R^2 + \gamma R^{n-2}(\cos n\phi - \alpha \sin n\phi)]\lambda^2$$
$$+ 2n\gamma R^n(\cos n\phi - \beta \sin n\phi) - n(n-2)\gamma^2 R^{2n-4} = 0, \tag{12}$$

or equivalently

$$(1+\alpha^2)\lambda^4 + 2[\mu + \alpha\nu - 2(1+\alpha\beta)R^2]\lambda^2 - 2nR^2[\mu + \beta\nu$$
$$- (1+\beta^2)R^2] - n(n-2)[(\mu - R^2)^2 + (\nu - \beta R^2)^2] = 0. \tag{13}$$

The structure of this equation is a consequence of the fact that the time-independent version of Eq. (2), written as a four-dimensional dynamical system in x, is equivariant with respect to the reversibility symmetry mentioned above, $(x, A) \to (-x, A)$. This condition translates into the requirement that if λ is a spatial eigenvalue so are $\bar{\lambda}$ and $-\lambda$. As a result the spatial eigenvalues fall into one of the

following four generic configurations [2]

configuration (1):	a quartet of complex eigenvalues
configuration (2):	the eigenvalues are all real
configuration (3):	two eigenvalues are real and two are imaginary
configuration (4):	the eigenvalues are all imaginary.

The transition from configuration (1) to configuration (2) corresponds to a Belyakov–Devaney point [26,27], with real eigenvalues $\pm\lambda$, each of double multiplicity. The Turing bifurcation, obtained above using standard stability analysis, corresponds to the transition between configuration (1) and configuration (4), and hence to purely imaginary eigenvalues $\pm ik_T$, each of double multiplicity. In the temporal context this bifurcation is called the reversible double-Hopf bifurcation with 1:1 resonance [28]. In contrast, at a saddle–node $\lambda = 0$, also twice, and this is so also at pitchfork bifurcations (see below). These situations correspond to the transition between configuration (3) and configuration (2) or (4).

The reversibility symmetry also constrains the spatial Floquet multipliers. If a symmetric spatially periodic orbit has a Floquet multiplier Λ then Λ^{-1} must also be a multiplier of the orbit. It follows that in a four-dimensional system there is always a pair of Floquet multipliers $\Lambda = +1$, and the remaining two must lie in one of three configurations

configuration (I):	both lie on the real axis, $\Lambda > 0$
configuration (II):	both lie on the unit circle
configuration (III):	both lie on the real axis, $\Lambda < 0$.

Formulating the problem as a steady state bifurcation problem in space has several advantages. In particular, the spatial eigenvalues provide necessary conditions for the presence of homoclinic and heteroclinic orbits between homogeneous equilibria. Since such orbits can only connect hyperbolic equilibria, with at least one unstable spatial eigenvalue and at least one stable spatial eigenvalue, homoclinics are only expected in cases (1) and (2); in case (3) homoclinics may be present at isolated parameter values. Moreover, it is now possible to establish the *bifurcation* of such states from the homogeneous state. Thus a pitchfork bifurcation of homogeneous states is associated with the simultaneous bifurcation of a homoclinic orbit (subcritical pitchfork) or a simultaneous bifurcation of a heteroclinic orbit (supercritical pitchfork). Likewise a saddle–node bifurcation of a homogeneous state is associated with the bifurcation of a homoclinic orbit. A subcritical Turing bifurcation producing periodic states is associated with a pair of subcritical branches of homoclinic orbits resembling wavepackets with characteristic wavenumber k_T. These differ in their spatial phase, with one branch containing solutions with local maxima in the symmetry plane and the other containing local minima. In contrast, a supercritical Turing bifurcation produces periodic states together with homoclinics to such states (see Appendix). Eckhaus bifurcations of periodic states also lead to (a pair of) homoclinics to the periodic state; these typically resemble holes in the periodic state and once again differ in their spatial phase [29]. The existence of these states can be established either using multiple scale methods near the corresponding bifurcations [30], or using normal form theory for reversible systems [28]. In the following we explore the behavior of these states as a function of the parameters focusing on situations where new types of behavior arise. We mention that all of the above solutions are invariant under reflection with respect to a suitable origin x_0 (i.e., $A(2x_0 - x) = A(x)$, localized states) or under the combined action of reflection followed by the operation $(x, A) \to (x, Ae^{2\pi i/n})$ (fronts). Solutions that break reflection symmetry ($A(2x_0 - x) \neq A(x)$, all x_0) generally drift and will not be considered.
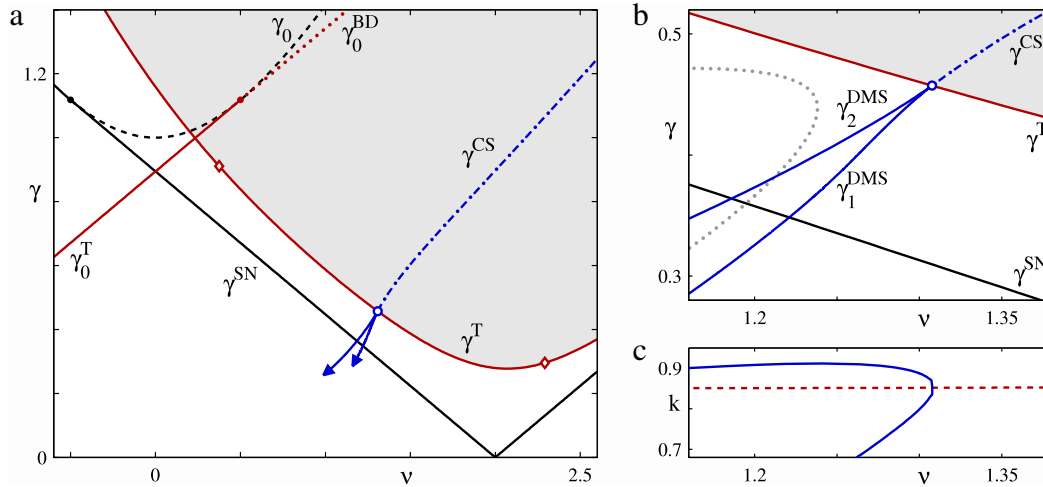
Fig. 1. (a) The (ν, γ) plane for Eq. (2) when $\alpha = -2$, $\beta = 2$, and $\mu = 1$. The curve γ_0 is plotted as a solid line in $\nu < \nu_\beta$ where the bifurcation to the uniform phase-locked states is supercritical, and dashed in $\nu > \nu_\beta$ where it is subcritical. The (solid) line γ_0^T in $\nu < \nu_\alpha$ represents a Turing bifurcation on $A = 0$; the (dotted) line γ_0^{BD} in $\nu > \nu_\alpha$ is the line of Belyakov–Devaney points on $A = 0$. The Turing bifurcation of A^+ at γ^T is supercritical between the locations indicated by $\diamond$, and subcritical elsewhere. The shaded region contains the stable spatially homogeneous state A^+. The heteroclinic cycle forms along the dot–dashed line γ^{CS}. (b) Detail near the codimension-two point $(\nu^*, \gamma^*) \simeq (1.3077, 0.4573)$, marked with an open circle, where collapsed snaking turns into defect-mediated snaking within $\gamma_1^{DMS} < \gamma < \gamma_2^{DMS}$. The dotted line shows the pinning region $\gamma_1^{HS} < \gamma < \gamma_2^{HS}$ containing regular homoclinic snaking. (c) The solid line shows the wavenumber range included in defect-mediated snaking as a function of ν. The dashed line shows $k_T(\nu)$. The wavenumber range shrinks to $k_T(\nu^*)$ as ν increases towards ν^*.

3. The 2:1 resonance

In this section we examine solutions to Eq. (2) for the case $n = 2$, the 2:1 resonance. In this case, the equation always has the trivial solution $A = 0$ in addition to the nontrivial homogeneous states discussed above. When two nonzero homogeneous solutions are present, we use the notation A^+/A^- to refer to solutions with larger/smaller R. The phase symmetry guarantees that all nontrivial (homogeneous or inhomogeneous) solutions come in pairs: if $A(x)$ is a solution so is $-A(x)$. To deal with the resulting ambiguity we choose whenever possible solutions with $V(0) \leq 0$, where $V(x) \equiv \text{Im} A(x)$. Throughout this section we adopt the parameter values $\alpha = -2$, $\beta = 2$ and $\mu = 1$, corresponding to Region V^+ in the classification scheme of [30].

Since $\mu > 0$ the $A = 0$ state is unstable, although it undergoes a steady state pitchfork bifurcation to homogeneous states at

$$\gamma = \gamma_0 \equiv \sqrt{\mu^2 + \nu^2}; \tag{14}$$

when $\nu < \nu_\alpha \equiv -\mu/\alpha$ this bifurcation is preceded by a steady state Turing bifurcation at

$$\gamma = \gamma_0^T \equiv \frac{|\nu - \mu\alpha|}{\sqrt{1 + \alpha^2}} \tag{15}$$

to a spatially periodic state with wavenumber

$$k = k_{0T} \equiv \sqrt{\frac{\alpha(\nu - \nu_\alpha)}{1 + \alpha^2}} \tag{16}$$

as obtained from the equation for spatial eigenvalues of $A = 0$,

$$(1 + \alpha^2)\lambda^4 + 2\alpha(\nu - \nu_\alpha)\lambda^2 + \mu^2 + \nu^2 - \gamma^2 = 0, \tag{17}$$

on demanding that $\lambda = 0$ and $\lambda = \pm ik_{0T}$, respectively.

In Fig. 1(a) we show the (ν, γ) parameter plane for these parameter values. The figure shows the curves $\gamma = \gamma_0, \gamma_0^T$ of bifurcations on the trivial $A = 0$ state. These two lines are tangent at $\nu = \nu_\alpha = 0.5$. Beyond $\nu = \nu_\alpha$ the line γ_0^T represents Belyakov–Devaney points and is labeled γ_0^{BD}. In addition, $\gamma = \gamma_0$ is tangent to the line of saddle–nodes computed from Eq. (7) and given by $\gamma = \gamma^{SN} \equiv \frac{|\nu - \beta\mu|}{\sqrt{1 + \beta^2}}$; this tangency occurs at $\nu = \nu_\beta \equiv -\mu/\beta = -0.5$. When $\nu > \nu_\beta$ the homogeneous states A^- states appear via a subcritical bifurcation from $A = 0$ at $\gamma = \gamma_0$

and are unstable. These states annihilate with the large amplitude homogeneous states A^+ at $\gamma = \gamma^{SN}$ thereby defining the region of bistability between the two homogeneous states $A = 0$ and $A = A^+$. In contrast, when $\nu < \nu_\beta$ the A^- states and the saddle–node bifurcation are absent, and the A^+ states bifurcate directly from $A = 0$ at γ_0 and do so supercritically. Finally, the figure also shows the line $\gamma = \gamma^T$ corresponding to the Turing bifurcation on $A = A^+$ as determined from Eq. (10). Details may be found in [30].

3.1. Homoclinic snaking

In this section we describe the behavior of the branches identified above when these are followed in parameter space. In general we use γ as the bifurcation parameter and show the resulting solution branches for several fixed values of ν. Fig. 2 shows the bifurcation diagram of stationary solutions at $\nu = 1.2 < \nu^*$, plotted in terms of the L^2 norm N defined as

$$N = \sqrt{\frac{1}{\ell} \int_{-\ell/2}^{\ell/2} \{|A(x)|^2 + |A_x(x)|^2\} dx}, \tag{18}$$

where ℓ is the large but finite domain used in the computation. The branches of spatially homogeneous solutions in this figure are characteristic of the entire range of ν considered in this section. In particular, since $\nu > \nu_\alpha$, the four spatial eigenvalues of the $A = 0$ state are real in $\gamma_0^{BD} < \gamma < \gamma_0$ (configuration (2)) while for $\gamma < \gamma_0^{BD}$ they are complex (configuration (1)). Moreover, since $\nu > \nu_\beta$ the nontrivial homogeneous state A^- emerges from the $A = 0$ state in a subcritical bifurcation at $\gamma = \gamma_0$ and coalesces with the A^+ state in a saddle–node bifurcation at $\gamma = \gamma^{SN}$. In addition, the value of ν used in Fig. 2 lies in the range where the bifurcation at $\gamma = \gamma^T$ is supercritical, i.e., periodic states with wavenumber k_T bifurcate into $\gamma < \gamma^T$, with the A^+ branch in $\gamma > \gamma^T$ ($\gamma < \gamma^T$) temporally stable (unstable). Accompanying this bifurcation is a continuum of supercritical spatially periodic branches (not shown in the figure) with wavenumbers in a neighborhood of k_T that also bifurcate from A^+ into $\gamma < \gamma^T$. Each fixed-k branch undergoes one or more saddle–node bifurcations, and may pass through $\gamma = \gamma^T$ several times. When both γ and k are viewed as bifurcation parameters, the continuum of branches forms a surface of spatially periodic states with several folds (i.e., lines of saddle–nodes) and
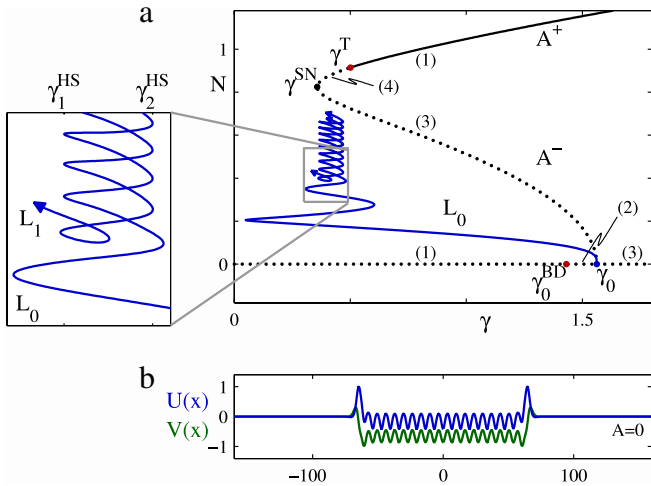
Fig. 2. (a) Bifurcation diagram corresponding to the $\nu = 1.2 < \nu^*$ slice of Fig. 1, where the branch of localized states undergoes homoclinic snaking. Solid (dotted) lines correspond to stable (unstable) homogeneous solutions, with the labels indicating the corresponding spatial eigenvalue configuration. The branches L_0 and L_1 of localized states are everywhere unstable but are plotted as solid lines for clarity. The inset shows the detailed behavior of L_0 and L_1. The limiting values for the saddle–node bifurcations far up the homoclinic snaking branches are $\gamma_1^{HS} \simeq 0.3662$ and $\gamma_2^{HS} \simeq 0.4689$. The L_1 branch exits this snaking region at small amplitude and enters a second homoclinic snaking region (not shown) in $0.3289 \leq \gamma \leq 0.3659$. (b) A sample solution high up the L_0 branch.

possible cusps. We use the notation $A_P(x; \gamma, k)$ to refer to solutions on this surface.

The behavior of the branches of spatially localized solutions depends crucially on the value of ν. Fig. 2 includes two distinct branches of localized solutions, labeled L_0 and L_1. The profiles along each of these branches are invariant under the reversibility symmetry of the system and resemble a slug of a uniform amplitude spatially periodic pattern $A_P(x; \gamma, k)$ connected by a pair of fronts to the trivial background state $A = 0$ as $|x| \to \infty$. The L_0 (L_1) branch includes all solutions with local minima (maxima) in $V(x)$ at $x = 0$, subject to the convention mentioned above that we choose the overall sign of $A(x)$ such that $V(0) \leq 0$.

Each of the branches L_0 and L_1 exhibits homoclinic snaking, a reference to the back-and-forth motion of the branch as it undergoes an infinite sequence of saddle–node bifurcations. The left

saddle–nodes approach a limiting value γ_1^{HS} and the right saddle–nodes approach a different limiting value γ_2^{HS}, resulting in an infinite multiplicity of distinct localized states within the snaking (or pinning) region $\gamma_1^{HS} \leq \gamma \leq \gamma_2^{HS}$. Fig. 3 shows in more detail the variation of the profiles along the two branches. In each case, one full back-and-forth cycle up the snaking branch pushes each of the fronts symmetrically one wavelength farther from the midpoint, thereby increasing the overall width of the state by twice this wavelength.

The pattern within the localized state always matches one of the solutions $A_P(x; \gamma, k)$ on the surface of spatially periodic states. In regular homoclinic snaking the pattern is always associated with a segment of the appropriate fixed-k branch that is separated from onset (near A^+) by at least one saddle–node (Fig. 4(a)), and always has Floquet multipliers in configuration (I). The wavenumber of the selected pattern within the localized state varies across the pinning interval, as shown in Fig. 5. The wavenumber variation along all branch segments extending from γ_1^{HS} to γ_2^{HS} is the same (curve C') and likewise for all segments extending from γ_2^{HS} to γ_1^{HS} (curve C). Thus the wavenumber selection along these two types of segments differs, although the wavenumbers at the end points γ_1^{HS} and γ_2^{HS} must, of course, match, i.e., the selected wavenumber $k(\gamma)$ must form a closed curve (Fig. 5).

Homoclinic snaking can be understood from the perspective of spatial dynamics as follows. The localized states that make up the snaking branches correspond to reversible homoclinic orbits which resemble heteroclinic cycles to the $A = 0$ state. Each cycle can be decomposed into two pieces: a heteroclinic connection from $A = 0$ to a reversible orbit $A_P(x; \gamma, k)$, and the symmetric heteroclinic orbit from $A_P(x; \gamma, k)$ back to $A = 0$. In the parameter regime of interest the spatial eigenvalues of $A = 0$ are in configuration (1), implying that the unstable manifold of this fixed point is two-dimensional, while the Floquet multipliers of the relevant periodic orbit $A_P(x; \gamma, k)$ are in configuration (I), implying that the center-stable manifold of this state is three-dimensional. In the four-dimensional phase space of the spatial dynamical system the intersection of these two manifolds is of codimension zero (i.e., structurally stable) and determines the selected wavenumber $k(\gamma)$. The first and last tangencies between these two manifolds occur at γ_1^{HS} and γ_2^{HS}, where pairs of heteroclinic orbits are created or destroyed in saddle–node bifurcations, as suggested by Fig. 5. A detailed explanation of
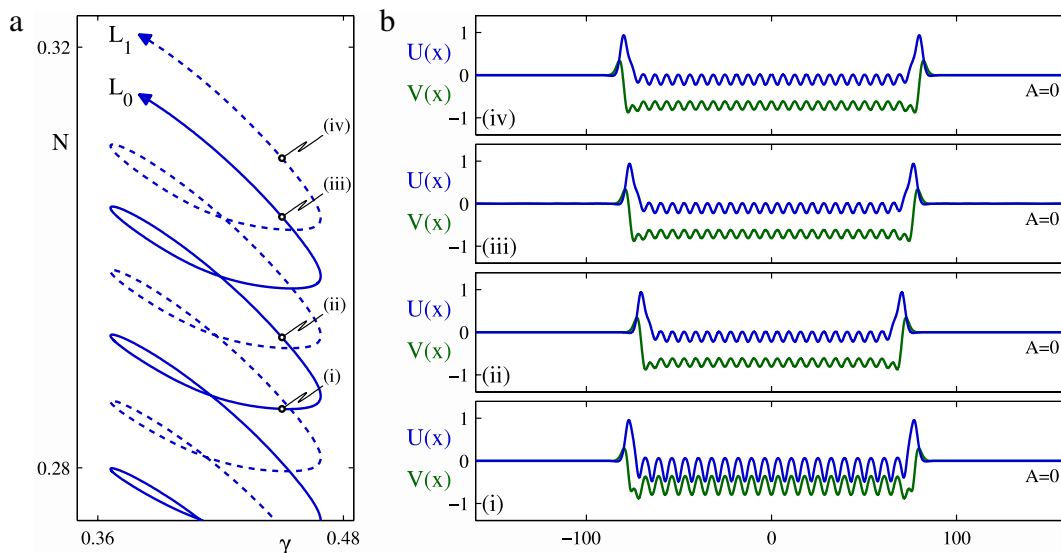

Fig. 3. (a) Detail of the snaking branches in Fig. 2. The L_0 (L_1) branch is plotted as a solid (dashed) line. (b) Frames (i)–(iii) show profiles on L_0 (minima of $V(x)$ at $x = 0$) while (iv) shows a profile on L_1 (maximum of $V(x)$ at $x = 0$).
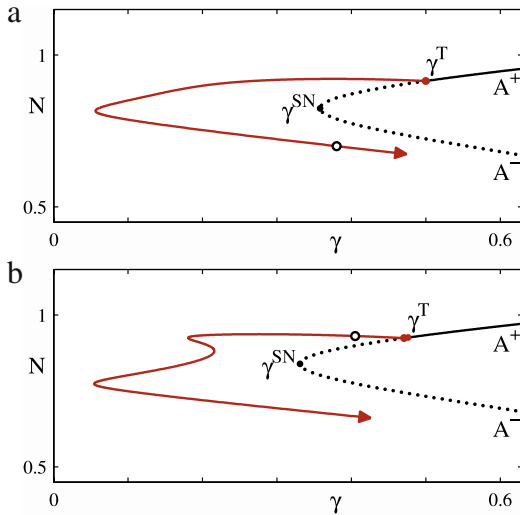
Fig. 4. (a) Bifurcation diagram showing the $k = 0.8708$ branch of spatially periodic states for the parameter values at which Fig. 2 reveals homoclinic snaking. This wavenumber matches the pattern within localized states when $\gamma = 0.38$. The open dot indicates that the included pattern occurs on the segment of the branch separated from the Turing bifurcation by a saddle–node. (b) Bifurcation diagram showing the $k = 0.7937$ branch of spatially periodic states for the parameter values at which Fig. 7 reveals defect-mediated snaking. This wavenumber matches the pattern within localized states when $\gamma = 0.405$. The open dot indicates that the pattern incorporated into the localized state is selected from the segment of branch closest to the Turing bifurcation.
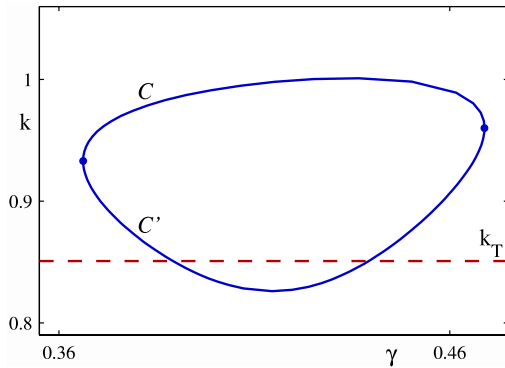
Fig. 5. The wavenumber k of the spatially periodic pattern within the localized states at $\nu = 1.2$ in the interval $\gamma_1^{HS} < \gamma < \gamma_2^{HS}$. As one traces 'up' a snaking branch, the smaller wavenumber (curve C') is measured along the segments which extend from γ_1^{HS} to γ_2^{HS}, as in profile (i) in Fig. 3; the larger wavenumber (curve C) is measured along the segments which extend from γ_2^{HS} to γ_1^{HS}, as in profiles (ii), (iii) and (iv) in Fig. 3. For reference the dashed line indicates the wavenumber k_T of the initial instability at γ^T. The Floquet multipliers in this region of the surface of spatially periodic states are always in configuration (I).

how the bifurcation structure of heteroclinic orbits generates homoclinic snaking is provided in Ref. [10]. However, the precise mechanism determining $k(\gamma)$ is only understood in systems with a conserved spatial Hamiltonian [31] and, in the present system, remains unclear.

Each of the snaking branches in Fig. 2 exits the bottom of the pinning region when the width of the localized state becomes sufficiently small, containing just two to three wavelengths of the selected pattern. The L_0 branch extends to larger values of γ as the amplitude of the solution decreases, and eventually terminates in a pitchfork bifurcation of the $A = 0$ state at $\gamma = \gamma_0$. This bifurcation was studied in Ref. [30]. In contrast, the L_1 branch exits the pinning interval in the direction of decreasing γ and enters a second pinning region where it again undergoes homoclinic snaking (not shown). The wavenumbers selected in this region by
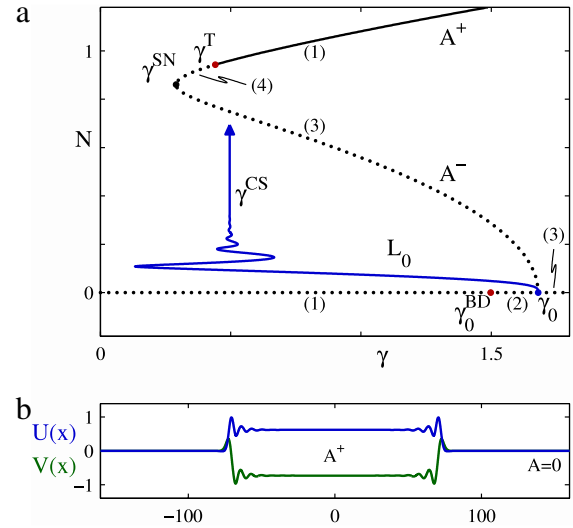
Fig. 6. (a) Bifurcation diagram corresponding to the $\nu = 1.35 > \nu^*$ slice of Fig. 1, where the branch of localized states undergoes collapsed snaking towards $\gamma = \gamma^{CS} \simeq 0.4962 > \gamma^T$. The localized states are everywhere unstable but are shown as a solid line. The remaining solid (dotted) lines correspond to stable (unstable) homogeneous states. (b) A sample solution far up the collapsed snaking branch, at $\gamma \approx \gamma^{CS}$.

the fronts at either end differ from the wavenumbers shown in Fig. 5. Additional snaking regions may also be present.

3.2. Collapsed snaking

Consider next the behavior of solutions at $\nu = 1.35 > \nu^*$, shown in Fig. 6. The behavior of the spatially homogeneous branches is qualitatively similar to the previous case including the relative position of the bifurcations, the temporal stability, and the spatial eigenvalue structure. In this case there is only a single branch of localized solutions homoclinic to the $A = 0$ state (modulo the symmetry $(x, A) \to (x, -A)$). Since the branch originates at γ_0 we again label it L_0. As in the previous case the L_0 branch is associated with a subcritical pitchfork bifurcation of the $A = 0$ state at $\gamma = \gamma_0$ and undergoes an infinite sequence of saddle–node bifurcations far from onset. However, in this case the branch exhibits *collapsed* snaking as the separation in γ between consecutive saddle–nodes decreases exponentially, and both the left and right saddle–nodes asymptote to the same limiting value of $\gamma = \gamma^{CS} > \gamma^T$ [30,32]. The profiles high up the collapsed snaking branch spend considerable 'time' in a neighborhood of the homogeneous state A^+, and resemble a heteroclinic cycle from $A = 0$ to A^+ and back again. The limit $\gamma = \gamma^{CS}$ corresponds to the (codimension-one) point at which a heteroclinic orbit connecting the fixed points $A = 0$, A^+ is present. The back-and-forth approach of the collapsed snaking branch to this limiting value is a direct consequence of the fact that the spatial eigenvalues of A^+ at γ^{CS} are complex (configuration (1)), as discussed in [32]. These eigenvalues are visible in the form of decaying oscillations in $U(x)$ and $V(x)$ as $x \to 0^-$ (and the growing oscillations for $x > 0$). Elsewhere in the parameter space of Eq. (2) there are regions where the spatial eigenvalues of the A^+ state at the limit point γ^{CS} are real (configuration (2)); in this case the profiles $U(x)$ and $V(x)$ lack spatially oscillating tails and the branch L_0 collapses monotonically in γ without any (asymptotic) saddle–node bifurcations [30].

3.3. Defect-mediated snaking

The bifurcation diagram for steady solutions of Eq. (2) at an intermediate value of ν, $\nu = 1.26 < \nu^*$, is shown in Fig. 7. Here we
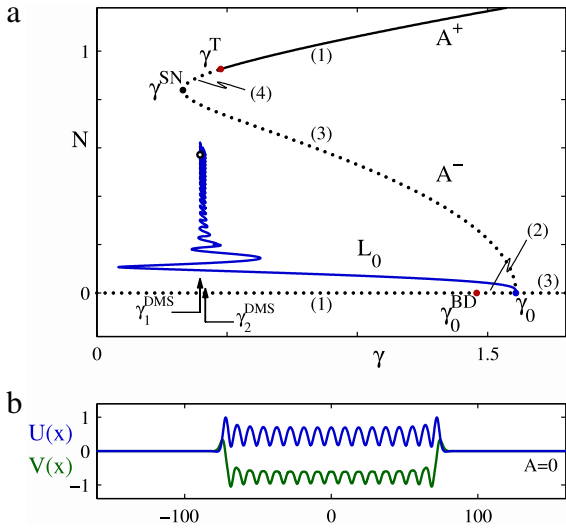
Fig. 7. (a) Bifurcation diagram corresponding to the $\nu = 1.26$ slice of Fig. 1, where the branch of localized states undergoes defect-mediated snaking. The localized states within the pinning interval $\gamma_1^{DMS} \leq \gamma \leq \gamma_2^{DMS}$, where $\gamma_1^{DMS} \simeq 0.3966$ and $\gamma_2^{DMS} \simeq 0.4167$, are all unstable. The remaining solid (dotted) lines represent stable (unstable) homogeneous solutions. (b) A sample solution high up the snaking branch.

find that while the behavior of the spatially homogeneous states $A = 0$ and $A^{\pm}$ remains qualitatively similar to the previous two cases, the behavior of the localized states differs dramatically: a snaking branch L_0 of spatially localized states emerges from $A = 0$ at $\gamma = \gamma_0$ much as in regular homoclinic snaking but this time the partner branch L_1 is *absent*. Instead the L_0 branch combines elements from both the L_0 and L_1 branches in Fig. 2 and it does so via a distinct growth mechanism which we call *defect-mediated snaking* (DMS). When describing this mechanism we label the left and right limit values of the saddle–node bifurcations on either side of L_0 by γ_1^{DMS} and γ_2^{DMS}, respectively, and continue to refer to $\gamma_1^{DMS} \leq \gamma \leq \gamma_2^{DMS}$ as a pinning or snaking interval.

The growth of the localized states along the DMS branch is illustrated in Fig. 8. This branch contains two distinct families of states. The first of these are the uniform amplitude segments, where the profiles consist of slugs of a uniform amplitude spatially periodic pattern connected to the $A = 0$ background state by a pair of fronts, and therefore resemble the localized states found in regular homoclinic snaking. These segments extend from γ_2^{DMS} to γ_1^{DMS} as one moves up the DMS branch, and are shown in Fig. 8 using solid lines. The pattern within these localized states always matches one of the solutions $A_P(x; \gamma, k)$ from the surface of spatially periodic states. Unlike the case of regular homoclinic snaking, in defect-mediated snaking the patterns are always associated with a segment of the appropriate fixed-k branch which connects *monotonically* to A^+ (Fig. 4(b)). This section of the surface of periodic states is shown in Fig. 9. The boundary of the surface is formed by the neutral stability curve of the A^+ state. Shading is used to indicate the configuration of Floquet multipliers at each (γ, k). The patterns within the localized states always come from the Eckhaus-stable band, where the Floquet multipliers have configuration (I). In defect-mediated snaking, the curve of selected wavenumbers $k(\gamma)$ is 'S'-shaped and spans the entire width of the Eckhaus band, terminating at the boundaries where the Floquet multipliers transition to configuration (II).

Fig. 8 also shows that the DMS branch alternates between two types of uniform amplitude segments: those where $V(x)$ has a minimum at $x = 0$ and those where $V(x)$ has a maximum at $x = 0$. The corresponding profiles are labeled by their spatial phase Φ (see below), $\Phi = 0$ for the former and $\Phi = \pi$ for the latter. The single DMS branch in Fig. 8 therefore combines elements of both the L_0 and L_1 branches in Fig. 2.

The spatial dynamics explanation of the uniform amplitude segments of the DMS branch is similar to the previous explanation of regular homoclinic snaking. The localized states correspond to reversible homoclinic orbits which resemble heteroclinic cycles from $A = 0$ to $A_P(x; \gamma, k)$ and back again. These are ultimately a consequence of the structurally stable intersection of the two-dimensional unstable manifold of the $A = 0$ fixed point and the three-dimensional center-stable manifold of the periodic orbit
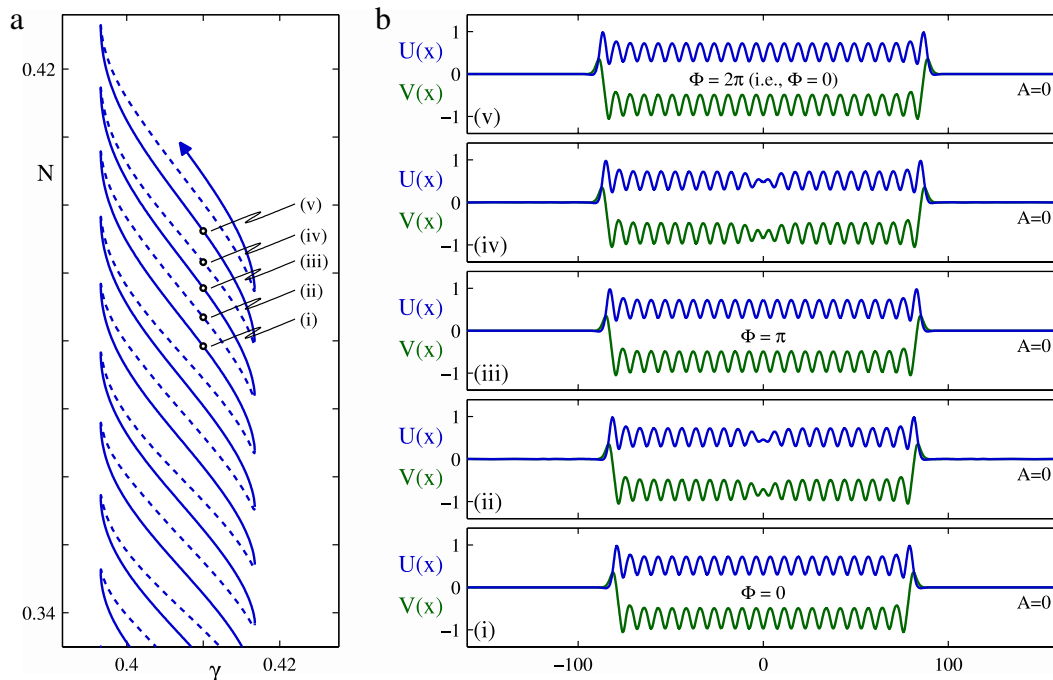

Fig. 8. (a) Detail of the L_0 snaking branch in Fig. 7. The uniform amplitude segments of the branch are shown as solid lines, while the defect segments are shown as dashed lines. (b) Five sample solutions, all at $\gamma = 0.41$. The spatial phase Φ is indicated for each profile on a uniform amplitude segment.
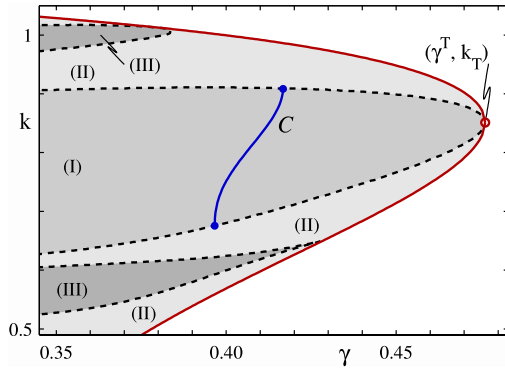
Fig. 9. Section of the surface of spatially periodic states for the parameters used in Fig. 7. The surface is bounded by the neutral stability curve of the A^+ state. The configuration of the Floquet multipliers in each shaded region is indicated. The curve C shows the wavenumber $k(\gamma)$ of the patterns included in defect-mediated snaking; this wavenumber spans the width of the Eckhaus band.

Fig. 10. The phase $\Phi(\gamma)$ of the solution across two complete turns of the snaking branch in Fig. 8(a). The phase varies monotonically across defect segments but remains constant on uniform amplitude segments. The labels mark the phases of the profiles shown in Fig. 8(b).

(two center directions plus one strong stable direction), combined with the reversibility symmetry of the system. In the case of defect-mediated snaking, the extent in γ of the heteroclinic connection is not determined by the first and last tangencies of these manifolds, but instead by a change in the dimensionality of one of the manifolds. In particular, the limits $\gamma_{1,2}^{\mathrm{DMS}}$ lie on the Eckhaus boundary where the periodic orbit loses its one strong stable direction so the heteroclinic orbit from $A = 0$ to $A_P(x; \gamma, k)$ must terminate.

The remaining segments in Fig. 8, plotted using dashed lines, are the defect segments. The profiles along these segments again correspond to reversible homoclinic orbits which resemble heteroclinic cycles to the $A = 0$ state. But here each cycle can be decomposed into *three* pieces: a heteroclinic connection from $A = 0$ to a reversible orbit $A_P(x; \gamma, k)$, a homoclinic connection from this orbit back to itself, and a heteroclinic connection from $A_P(x; \gamma, k)$ back to $A = 0$, cf. [33]. The spatially periodic states $A_P(x; \gamma, k(\gamma))$ associated with the defect segments are *identical* to those associated with the uniform amplitude segments at the same γ. Thus the plot of $k(\gamma)$ in Fig. 9 also applies along the defect segments. Likewise, the heteroclinic connections between $A = 0$ and $A_P(x; \gamma, k(\gamma))$ are the same along both the uniform amplitude and the defect segments (see Fig. 8). The only new feature along the defect segments is therefore the defect itself. The influence of this defect can be quantified by its spatial phase shift Φ. To define $\Phi(\gamma)$ we fix the spatial phase of the periodic orbits $A_P(x; \gamma, k)$ so that $V_P(x; \gamma, k) = \mathrm{Im}\, A_P(x; \gamma, k)$ has a local minimum at $x = 0$ and define $A_D(x; \gamma)$ to be the orbit with a defect centered at $x = 0$ which is homoclinic to $A_P(\cdot; \gamma, k(\gamma))$. Then $\Phi(\gamma)$ satisfies

$$\lim_{x \to \infty} A_D(x; \gamma) = A_P\left(x - \frac{\Phi(\gamma)}{k(\gamma)}; \gamma, k(\gamma)\right). \tag{19}$$

With this definition, a uniform profile with local minimum (maximum) in $V_P(x; \gamma, k)$ at $x = 0$ has phase $\Phi = 0$ ($\Phi = \pi$), and the total phase shift from $x \to -\infty$ to $x \to +\infty$ of a pattern with a defect relative to one without a defect is 2Φ. The phase $\Phi(\gamma)$ of the solution along two complete turns of the DMS branch is plotted in Fig. 10. The phase is constant along the uniform amplitude segments (either $\Phi = 0$ or $\Phi = \pi$) and increases by π across each defect segment, indicating the insertion of one extra wavelength into the pattern. The variation in phase across the pinning region is slightly different for defect segments which increase Φ from 0 to π and for those which increase Φ from π to 2π. We mention that the phase shown in the figure is determined empirically by examining the broad localized states found far up the defect-mediated snaking branch, rather than by computing the
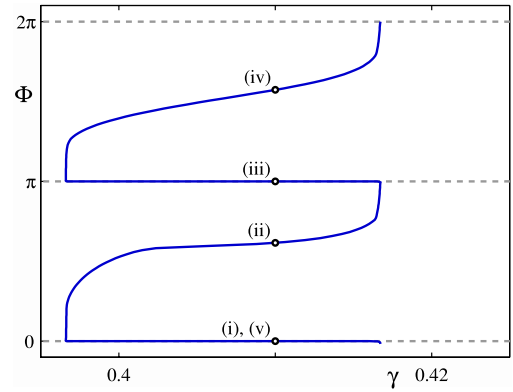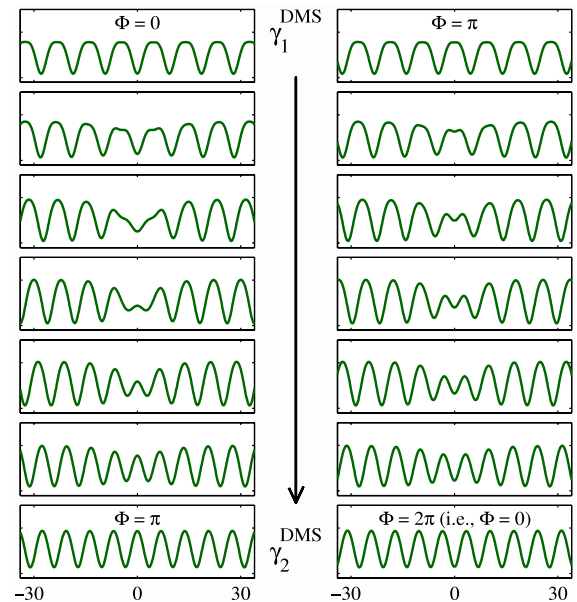

Fig. 11. Profiles from the defect segments across the snaking region of Fig. 8. The plot range is truncated to focus on the changes in $V(x)$ near the center of the domain at $x = 0$. The direction of increasing γ is indicated by an arrow, with the upper (lower) frames taken at the left (right) boundary of the snaking region.

actual homoclinic orbit $A_D(\cdot; \gamma)$. The defect is typically only a few wavelengths wide so the limit in Eq. (19) converges rapidly and $\Phi(\gamma)$ is well approximated by our method.

Fig. 11 shows in detail the variations of the profile along each type of defect segment. In each case, as γ increases across the pinning region the defect forces the central extremum to undergo "tip-splitting", thereby squeezing in an extra half wavelength on either side of $x = 0$ (i.e., one wavelength overall). As a result the localized state grows *from the center* rather than from the outside as occurs in regular homoclinic snaking, and with each wavelength insertion the existing "rolls" are pushed aside.

The behavior along the defect segments can be understood from the perspective of spatial dynamics as follows. Each defect corresponds to a reversible homoclinic orbit to a periodic orbit. Within the Eckhaus band the center-stable manifold of a periodic orbit is three-dimensional. The symmetric section of the four-dimensional phase space is two-dimensional. Hence, there is a continuous family of defects at each γ parameterized by the wavenumber k of the background periodic orbit. However, the wavenumber $k(\gamma)$ of the periodic orbits relevant in DMS is already
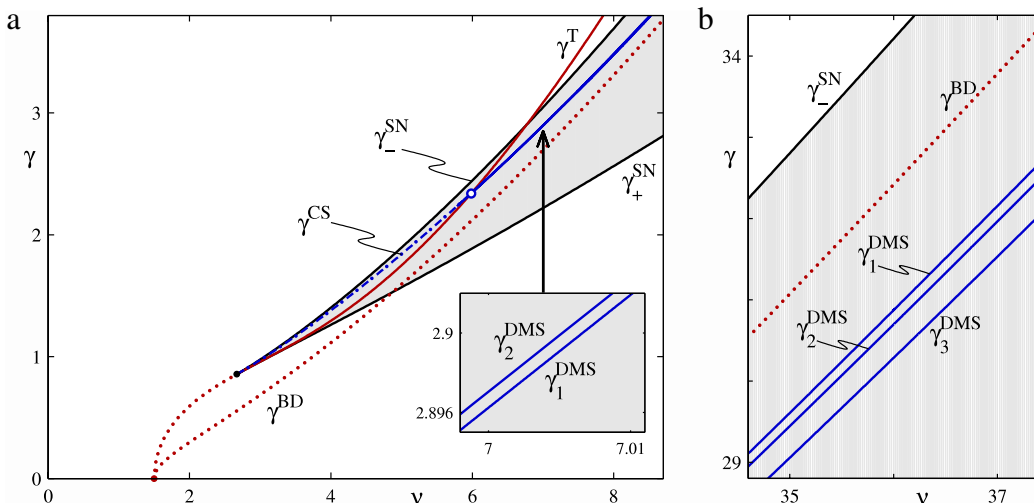
Fig. 12. (a) The critical curves and limits of snaking regions in the (ν, γ) plane. The lines $\gamma_{\pm}^{SN}$ delimit the region with three homogeneous equilibria while the line γ^T corresponds to Turing bifurcations on A^+. Belyakov–Devaney points on A^- occur along the line γ^{BD}. The transition from collapsed snaking at γ^{CS} to defect-mediated snaking between γ_1^{DMS} and γ_2^{DMS} occurs at the codimension-two point $(\nu^*, \gamma^*) \approx (5.983, 2.339)$, marked with an open circle. (b) At larger ν, defect-mediated snaking has an additional limit γ_3^{DMS}.

selected by the front that connects it to $A = 0$ as $|x| \to \infty$. Thus the defect structure varies continuously as γ varies across the snaking region. In the Appendix we study the normal form for the supercritical Turing bifurcation at $\gamma = \gamma^T$ in order to understand the homoclinic-to-periodic solutions born there in greater detail. We conjecture that these homoclinics become involved in the defect-mediated snaking we observe farther from $\gamma = \gamma^T$ but have not studied this process in detail.

3.4. Persistence as ν varies

In this section we describe the variation of the snaking behavior due to changes in ν, with a particular focus on γ^{CS} in the case of collapsed snaking and $\gamma_{1,2}^{DMS}$ in the case of defect-mediated snaking. As originally shown in Ref. [30], the location of γ^{CS} always remains above γ^T but approaches this value as ν decreases. The codimension-two bifurcation where $\gamma^{CS} = \gamma^T$ occurs at (ν^*, γ^*) indicated in Fig. 1(a) and (b) by an open circle. As ν increases towards ν^* the width of the pinning region containing defect-mediated snaking decreases, simultaneously with the wavenumber range of the periodic patterns within the localized states (Fig. 1(c)). At ν^* the system undergoes a smooth transition to collapsed snaking. Viewed from the other direction the heteroclinic connection between $A = 0$ and A^+ changes smoothly to a heteroclinic connection between $A = 0$ and a solution $A_P(x; \gamma, k)$ from the surface of spatially periodic states that emerges from A^+ near γ^T. A related transition occurs in the reversible Shil'nikov–Hopf bifurcation. In the present case this transition is nonhysteretic because the Turing bifurcation at γ^T remains supercritical as ν decreases through ν^*, and because the periodic orbits involved in defect-mediated snaking correspond to periodic states near the Turing bifurcation at $\gamma = \gamma^T$ rather than those separated from it by a saddle–node (Fig. 4).

The dotted line in Fig. 1(b) shows the width $\gamma_1^{HS} < \gamma < \gamma_2^{HS}$ of the pinning region associated with the regular homoclinic snaking shown in Fig. 2. We see that this region comes into being at a fold, i.e., this region does not originate in a 1:1 reversible Hopf bifurcation in space as in other systems known to the authors but resembles instead the behavior identified in the generalized Swift–Hohenberg equation far from the 1:1 spatial resonance [6]. The relation, if any, between regular homoclinic snaking in Eq. (2) and defect-mediated snaking in this equation remains unknown.
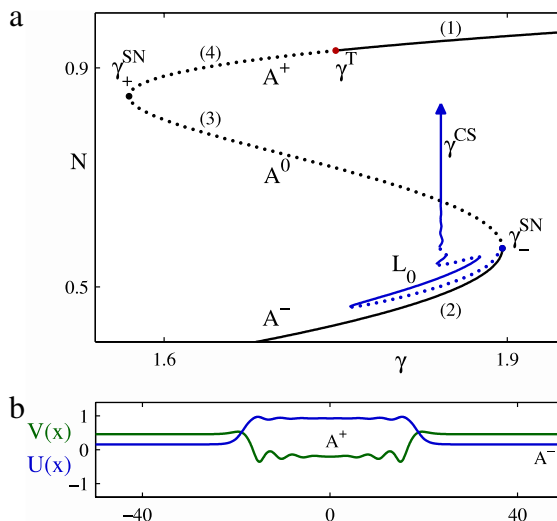

Fig. 13. (a) Bifurcation diagram corresponding to the $\nu = 5$ slice of Fig. 12, where the branch of localized states undergoes collapsed snaking towards $\gamma = \gamma^{CS} \approx 1.842$. The branch of localized states is computed on a domain of half-length $\ell/2 = 50$. Stable (unstable) segments are shown in solid (dashed) lines. For clarity, only the first three unstable segments are shown. On the homogeneous branches, solid (dotted) lines correspond to stable (unstable) solutions, and the labels indicate the spatial eigenvalue configurations. (b) A sample solution high up the L_0 branch.

4. The 1:1 resonance

In this section we focus on defect-mediated snaking in the case $n = 1$, i.e., in the 1:1 resonance. Unlike the case $n = 2$ studied in Section 3, $A = 0$ is no longer a solution and the phase symmetry $(x, A) \to (x, Ae^{2\pi i/n})$ is trivial. We adopt the parameter values $\alpha = -1.5$, $\beta = 6$ and $\mu = -1$ corresponding to Region V^- in the classification scheme of [34], and explore several values of the detuning ν. In addition to exhibiting bifurcation diagrams for stationary states we also examine their temporal stability.

As in the 2:1 resonance, localized states exist in the region of bistability, in this case between two distinct phase-locked states. Thus we focus on the parameter regime corresponding to the presence of three homogeneous equilibria (Fig. 12, region between lines $\gamma_{\pm}^{SN}$). The equilibrium with the smallest/middle/greatest L^2 norm will be denoted by $A^-/A^0/A^+$. In Region V^- the equilibrium
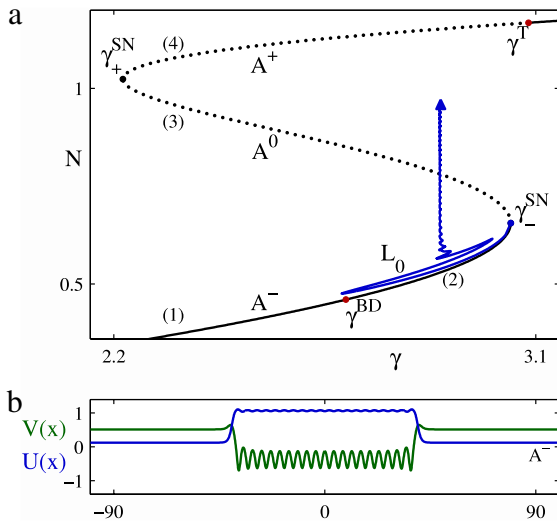
Fig. 14. (a) Bifurcation diagram corresponding to the $\nu = 7$ slice of Fig. 12, where the branch of localized states undergoes defect-mediated snaking between $\gamma_1^{DMS} \approx 2.8949$ and $\gamma_2^{DMS} \approx 2.8970$. Stability on the homogeneous branches is as in Fig. 13, but stability on L_0 is not indicated. (b) A sample solution high up the L_0 branch.

A^- is temporally stable [34] implying that all localized states considered here are embedded in a *stable* background. This is an important difference between the situation considered here and that considered in Section 3, and is a consequence of the fact that here $\mu = -1$ whereas in Section 3 $\mu = 1$.

The loci of bifurcation points of the equilibria in the (ν, γ) plane are shown in Fig. 12, together with the limits of the snaking region. These include the lines $\gamma_\pm^{SN}$ delimiting the region with three homogeneous equilibria and the lines γ^T and γ^{BD} corresponding respectively to Turing bifurcations on A^+ and Belyakov–Devaney points on A^-. In what follows, we study the branch of localized

states embedded in an A^- background, hereafter L_0. As explained in Section 2 these bifurcate from the lower saddle–node at γ_-^{SN}. For the chosen values of ν, there is always a supercritical Turing bifurcation on A^+ at γ^T.

4.1. Collapsed snaking

Fig. 13 shows the L_0 branch when $\nu = 5$. The branch undergoes collapsed snaking towards $\gamma = \gamma^{CS}$, where the solution profile approaches a heteroclinic cycle between A^- and A^+. The oscillatory approach to the codimension-one point γ^{CS} is a consequence of complex spatial eigenvalues of A^+ [32].

The localized states near γ_-^{SN} are temporally unstable. However, temporal stability changes at every saddle–node along the collapsed snaking branch. As a result, there is an infinite number of branch segments with stable localized states, located between the $(2i - 1)$-th and $2i$-th saddle–nodes, $i \in \mathbb{N}$. In contrast, in the 2:1 case the corresponding collapsed snaking does not produce stable localized states.

4.2. Two-limit defect-mediated snaking

The transition from collapsed snaking to defect-mediated snaking occurs as ν increases above ν^* (open circle in Fig. 12) and is similar to the corresponding transition in the 2:1 resonance.

Fig. 14 shows the bifurcation diagram at $\nu = 7 > \nu^*$. As a result the collapsed snaking in Fig. 13 is replaced by defect-mediated snaking within the interval $\gamma_1^{DMS} < \gamma < \gamma_2^{DMS}$. The detailed growth mechanism of the localized states in this region is shown in Fig. 15, and is essentially the same as in the DMS described in Section 3 for the 2:1 resonance. The DMS branch once again consists of uniform amplitude segments and defect segments, although this time the uniform amplitude segments extend from γ_1^{DMS} to γ_2^{DMS} as one follows the branch upwards, while the opposite occurs in Fig. 8. Despite this difference a localized state
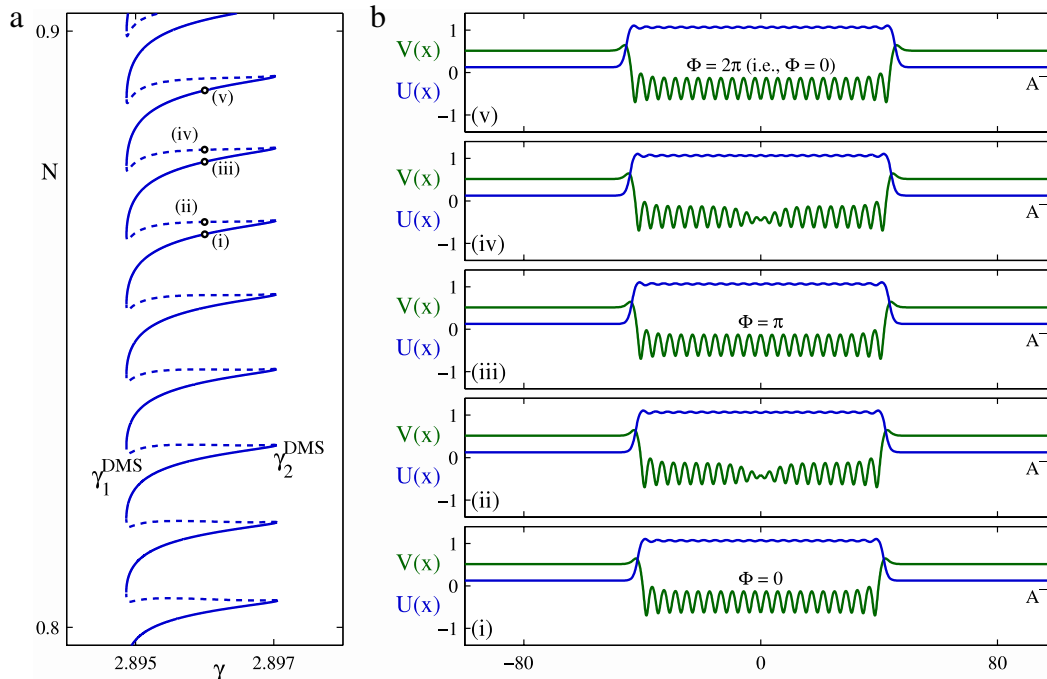

Fig. 15. (a) Detail of the L_0 snaking branch in Fig. 14. Temporally stable (unstable) segments are shown as solid (dashed) lines and coincide with uniform (defect) segments. (b) Five sample profiles at $\gamma = 2.896$. The spatial phase Φ is indicated for each profile on a uniform amplitude segment.
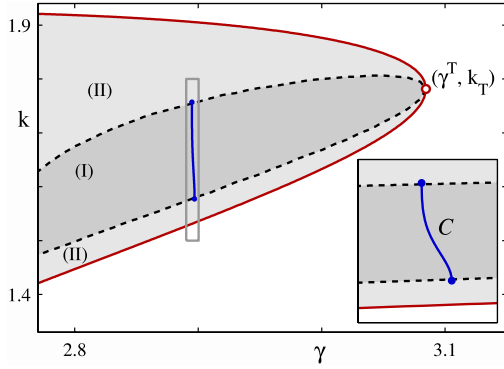
Fig. 16. Section of the surface of spatially periodic states for the parameters used in Fig. 14. The surface is bounded by the neutral stability curve of A^+. The configuration of the Floquet multipliers in each shaded region is indicated. The curve C shows the wavenumber $k(\gamma)$ of the patterns included in defect-mediated snaking at this value of the parameters and again spans the width of the Eckhaus band (inset).
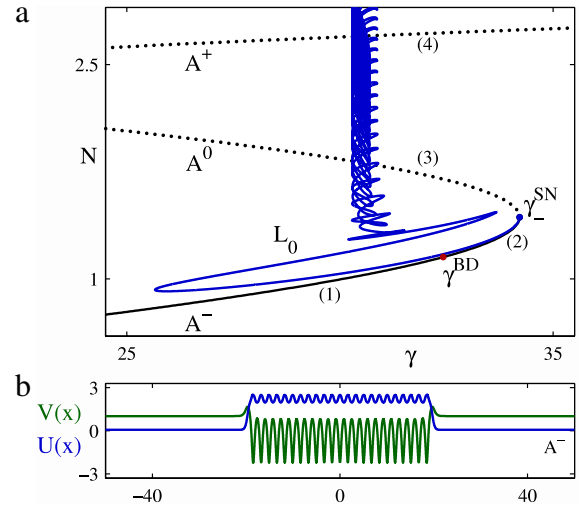

Fig. 17. (a) Bifurcation diagram corresponding to the $\nu = 36$ slice of Fig. 12, where the branch of localized states undergoes three-limit defect-mediated snaking. Stability on the homogeneous branches is as in Fig. 13, but stability on L_0 is not indicated. (b) A sample solution high up the L_0 branch.

on a uniform amplitude segment continues to resemble a periodic wave train connected to A^- by a pair of fronts, and a localized state on a defect segment resembles one on the uniform amplitude segment at the same γ, except for the presence of a defect in the middle of the wave train. Each time the branch passes through a defect segment, the defect inserts an extra wavelength at the center of the localized state exactly as in Fig. 11. Within the snaking region, the uniform amplitude segments are temporally stable, while all the defect segments are temporally unstable. This is as expected since the uniform amplitude segments lie between the $(2i - 1)$-th and $2i$-th saddle–nodes, $i \in \mathbb{N}$, and these are precisely the segments that are stable in the collapsed snaking shown in Fig. 13.

The wavenumber selection process across the snaking region, valid for both the uniform amplitude and defect segments, is illustrated in Fig. 16. The figure shows the wavenumber selected on the uniform segments high up the L_0 branch. As in the standard snaking scenario the wavenumber is constant across the localized structure at each γ and only depends on γ. However, in contrast to the regular case the selected wavenumber does not include the wavenumber k_T selected at γ^T because the DMS region is too far from γ^T at this value of ν.

As discussed already in Section 3.3 and illustrated further in Fig. 15, panels (ii) & (iv), the defects on successive defect segments differ. The defect at (ii)/(iv) is responsible for converting a local maximum/minimum of $V(x)$ at $x = 0$ into a local minimum/maximum at $x = 0$, by inserting in each case an extra wavelength at $x = 0$, exactly as in the 2:1 resonance (Fig. 8). Moreover, the phase $\Phi(\gamma)$ changes monotonically along the defect segments while remaining constant on the uniform amplitude segments exactly as in Fig. 10.

4.3. Three-limit defect-mediated snaking

Fig. 17 shows the solution behavior when $\nu = 36$. As in Fig. 14 the branch undergoes defect-mediated snaking, but this time the snaking region has three asymptotic limits, $\gamma_{1,2,3}^{DMS}$. The detailed growth mechanism of the localized states in this region is shown in Fig. 18 which shows one complete turn of the solution branch. As one follows the branch upwards, the uniform amplitude segments extend from γ_1^{DMS} through γ_3^{DMS} to γ_2^{DMS} (profiles (i) and (ii)), and the defect segments extend from γ_2^{DMS} through γ_3^{DMS} to γ_1^{DMS} (profiles (iii) and (iv)). As before, the defect segment is responsible for inserting an extra wavelength at the center of the localized state (compare (i) with (v)). Moreover, as in two-limit defect-mediated snaking, the limit points γ_1^{DMS} and γ_2^{DMS} define transition

points between the uniform amplitude and defect segments. The additional snaking limit γ_3^{DMS} is also associated with a qualitative change in the periodic state (compare the $U(x)$ profiles in (i) with (ii)). The details of this transition are shown in Fig. 19. The figure shows that this transition also occurs via "tip-splitting" but this time the tip-splitting occurs at $x = 0$ in $U(x)$ whereas the transition from profile (ii) to profile (v) takes place at $x = 0$ in $V(x)$ (Fig. 18). Neither transition is evident in the conjugate variable. Similar transitions take place on the next complete turn of the snaking curve, this time starting with state (v) and changing the minimum at $x = 0$ in $U(x)$ to a maximum when $\gamma \approx \gamma_3^{DMS}$, followed by a change of the maximum at $x = 0$ in $V(x)$ into a minimum along the corresponding defect segment. Despite the additional fold γ_3^{DMS}, the phase $\Phi(\gamma)$ again changes monotonically along the defect segments while remaining constant on the uniform amplitude segments.

The reason for the presence of the third limit point γ_3^{DMS} can be explained with the assistance of Fig. 20. This figure shows a section of the surface of spatially periodic states. Near (γ^T, k_T) the surface is smooth and single-valued as in Fig. 16. The limit points $\gamma_{1,2}^{DMS}$ lie on the boundaries of the Eckhaus-stable band, where the Floquet multipliers transition from configuration (I) to (II). As ν increases far above ν^* the curve of selected wavenumbers slides farther from the tip of the Eckhaus region at (γ^T, k_T) and eventually encounters a section of the surface of spatially periodic states where this surface is folded. Fig. 20 shows a section of this surface with two folds, one plotted as a solid line and the other as a dotted line. These folds meet in a cusp, marked by an open circle. The Floquet multipliers within each shaded region are indicated, although between the folds the Floquet multipliers are only indicated for the section of the surface with the largest L^2 norm, thus showing what one would see looking "down" on the surface from above. As for smaller values of ν, the curve $k(\gamma)$ of wavenumbers included in DMS extends between the boundaries of the Eckhaus band, but in this case the curve must trace around both folds and hence include patterns from the upper, middle, and lower sections of the folded surface; the presence of the third limit point γ_3^{DMS} in three-limit DMS is therefore a consequence of a global feature of the surface of spatially periodic states that is absent in the two-limit case. It follows that the spatial dynamics explanation of three-limit DMS is identical to the two-limit case. However, the
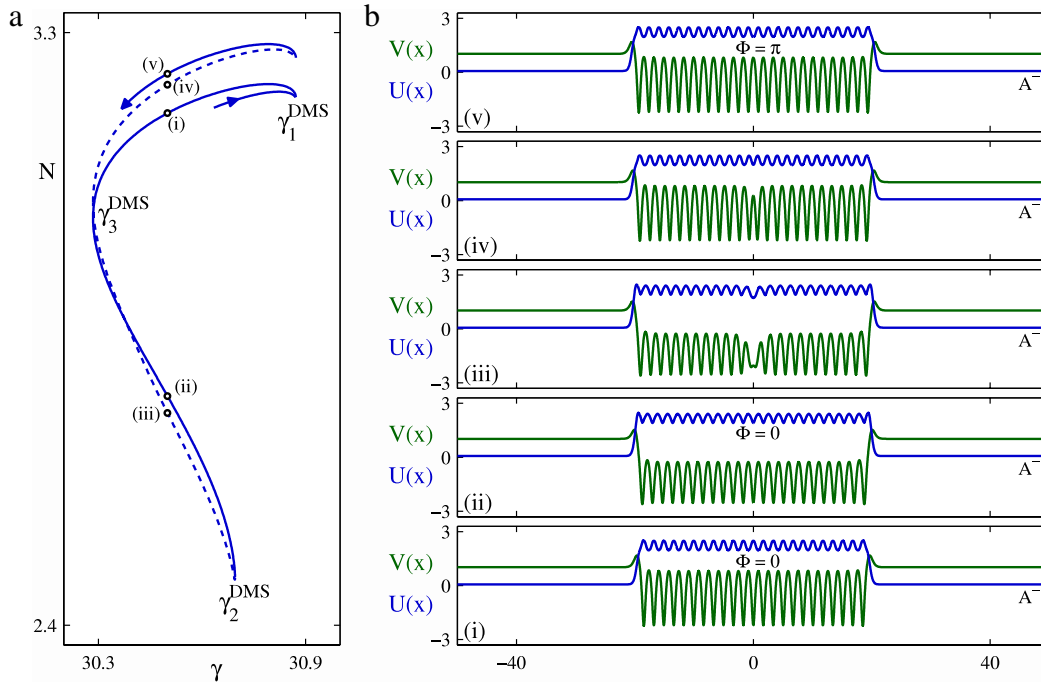
Fig. 18. (a) One complete turn of the snaking branch L_0 in Fig. 17. Solid (dashed) lines show uniform (defect) segments of the branch. Temporal stability is not indicated. The limiting values for the saddle–node bifurcations are $\gamma_1^{DMS} \approx 30.872$, $\gamma_2^{DMS} \approx 30.695$ and $\gamma_3^{DMS} \approx 30.285$. (b) Five sample solutions at $\gamma = 30.5$. The spatial phase Φ is indicated for profiles on the uniform amplitude segments. As Φ is defined in terms of $V(x)$, the change in the shape of $U(x)$ between (i) and (ii) does not change Φ.
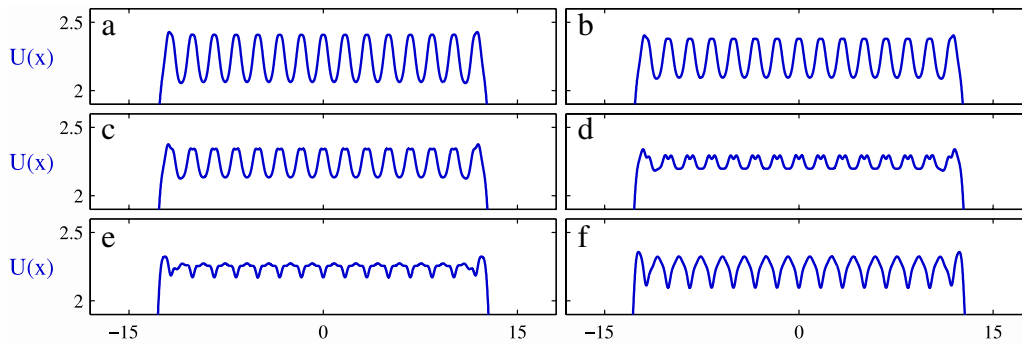

Fig. 19. Profiles $U(x)$ at six locations straddling a fold at γ_3^{DMS} on a uniform segment (solid line in Fig. 18) showing the transition from a state with a maximum at $x = 0$ (panel (a)) to one with a minimum at $x = 0$ (panels (d)–(f)) in the vicinity of the fold. During this transition $V(x)$ remains qualitatively unchanged. The locations (a)–(f) are indicated in Fig. 23.
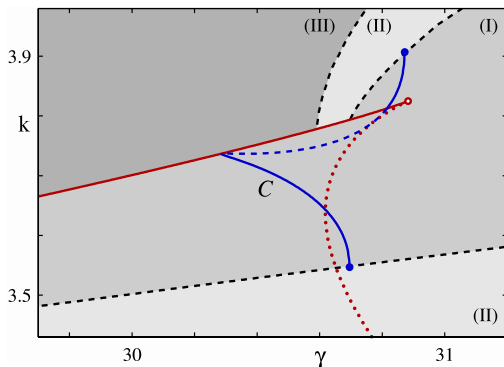

Fig. 20. A section of the surface of spatially periodic states for the parameters used in Fig. 17. Refer to the text for notation.

temporal stability properties of the uniform amplitude segments are, inevitably, more complicated in the three-limit case than in the two-limit case where these states are stable, as discussed next.

5. Time evolution

In this section, we describe the temporal evolution of the different unstable states associated with both two-limit and three-limit snaking.

5.1. The two-limit case: depinning

As discussed above, at $\nu = 7$ the localized states on the uniform amplitude segments in Fig. 15 are temporally stable for $\gamma_1^{DMS} < \gamma < \gamma_2^{DMS}$. The pair of fronts between the uniform and periodic states remains stationary in time, a phenomenon commonly referred to as pinning. However, outside the pinning region the fronts depin and begin to move. For $\gamma < \gamma_1^{DMS}$ Fig. 21(a) shows that the width of the localized state gradually decreases as the two fronts drift symmetrically inwards, ultimately leading to a final state consisting of a stable two-peak single-pulse state. In contrast, when $\gamma > \gamma_2^{DMS}$ the fronts drift apart allowing the structured state to invade the domain (Fig. 21(b)). This behavior is well-known from both variational systems such as the Swift–Hohenberg equation [6]
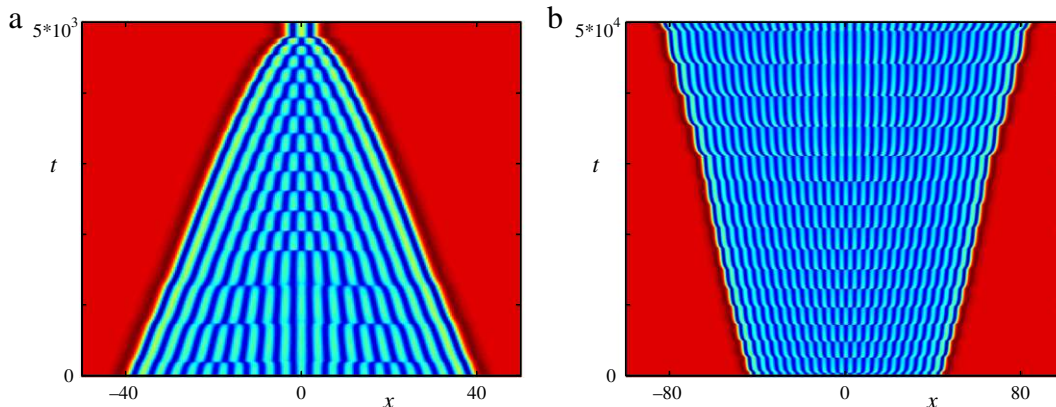
Fig. 21. Space–time plot of $V(x, t)$ for $\nu = 7$ showing the depinning of the fronts bounding a localized state at (a) 10^{-3} to the left of γ_1^{DMS} and (b) 10^{-4} to the right of γ_2^{DMS}. The final state in (a) is a steady localized state consisting of two wavelengths; in (b) the expanding state eventually fills the whole domain.

where it admits a natural explanation based on the free energies of the uniform and periodic states, and a variety of nonvariational systems such as binary mixture convection [3,4]. However, the evolution shown in Fig. 21(a) and (b) differs profoundly from that familiar from the Swift–Hohenberg equation and the convection systems cited above. In the latter the front represents a nucleation front, i.e., the front advances by nucleating new structures at a steady rate or retreats by annihilating structures also at a steady rate. Throughout the evolution the cells away from the front remain stationary and are altered (switched on or off) only by the passage of the front. This is because the eigenfunction responsible for the depinning of the front is strongly localized at the front or just outside it. In contrast, Fig. 21 reveals that in the present case the motion of the front is associated with a continuous drift of several cells near the location of the front without either nucleation of new cells in the front region or their destruction. Instead one finds that cells are progressively destroyed in an intermediate region between the front and the center of the structure, with the destruction zone gradually moving to the center once the structure becomes sufficiently narrow (Fig. 21(a)). Thus the behavior of the system takes the form of repeated phase slips generated by the Eckhaus instability [35], with the region where the phase slips take place drifting inward with approximately the speed of the front. This behavior is reversed in Fig. 21(b) where the fronts drift outward instead of inward. In this figure the phase slips occur initially in the center of the structure, at $x = 0$, but once the structure becomes broad enough the location of the phase slips splits into two locations which drift outwards more-or-less with the speed ν of the outer fronts.

Fig. 21(a) shows that as the fronts move inward the pattern is more-or-less uniformly compressed resulting in an average wavenumber k that increases with time. This progressive change in wavenumber triggers Eckhaus instability that is responsible for the elimination of a pair of rolls (one wavelength). After each phase slip the pattern relaxes again into a more-or-less uniform wavenumber state, but the continued motion of the fronts compresses the rolls again and triggers another phase slip. Evidently the speed of the fronts, ν, is related to the interval T between successive phase slips by the relation $\nu T \approx 2\pi/k$, where $k \approx k(\gamma_1^{DMS})$. Since ν varies as $|\gamma - \gamma_1^{DMS}|^{1/2}$ the phase slips occur with frequency $T^{-1} \sim |\gamma - \gamma_1^{DMS}|^{1/2}$. This relation is verified in Fig. 22(a). A similar relation, with γ_1 replaced by γ_2, holds for fronts that are moving apart (Fig. 22(b)). The nonzero intercepts on the horizontal axis are most likely due to the finite spatial extent of the wave train.

We have also examined the time evolution starting from the unstable defect branches. Here we find that the defect heals and the solution either grows into a state with an extra half wavelength
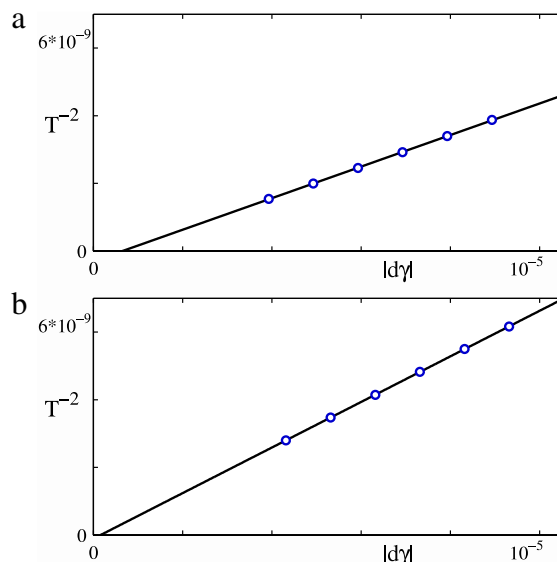

Fig. 22. Plots of $1/T^2$, where T is the time between the first two phase slips, as a function of the distance $|d\gamma|$ from the saddle–node for (a) $\gamma < \gamma_1^{DMS}$ and (b) $\gamma > \gamma_2^{DMS}$. The initial conditions are taken at the 71-st and 72-nd saddle–nodes, respectively, and the $|d\gamma|$'s are measured relative to the location of the 69-th and 74-th saddle–nodes. The solid lines show the best fit lines (a) $T^{-2} = 4.533 \times 10^{-4}|d\gamma| - 5.612 \times 10^{-10}$, and (b) $T^{-2} = 6.766 \times 10^{-4}|d\gamma| - 3.606 \times 10^{-10}$. Parameters: $\alpha = -1.5$, $\beta = 6$, $\mu = -1$, $\nu = 7$.

or it contracts into a state that is shorter by half a wavelength (on either side). The outcome appears to depend on whether the defect state is "closer" to the longer or the shorter uniform amplitude state, or equivalently whether γ lies in the right half of the pinning region or the left half, although it depends sensitively on the amplitude of the initial perturbation as well.

5.2. The three-limit case

When $\nu = 36$ there are three additional critical values of γ denoted by $\gamma_{A,B,C}$ separating the behaviors triggered by small amplitude perturbations of the localized states on a uniform amplitude segment. Fig. 23(a) indicates that for $\gamma_2^{DMS} < \gamma < \gamma_1^{DMS}$ (downward-pointing triangles), the fronts drift outward much like Fig. 21(b) and the domain is ultimately filled with a periodic state. This spatially periodic end state is time-independent and stable for $\gamma_2^{DMS} < \gamma < \gamma_A$ (filled triangles) but oscillates in time for $\gamma_A < \gamma < \gamma_1^{DMS}$ (unfilled triangles). In the interval $\gamma_3^{DMS} < \gamma < \gamma_2^{DMS}$ the branch of localized states has two parts, an upper part
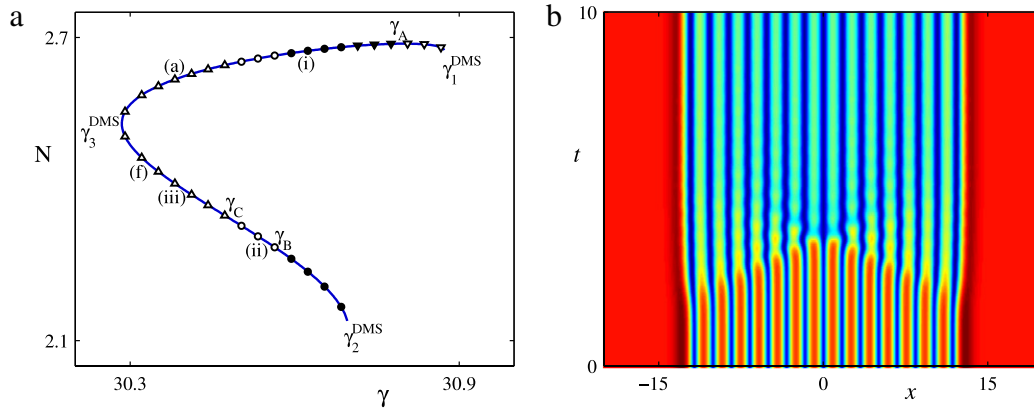
Fig. 23. (a) A branch of uniform amplitude localized states when $\nu = 36$ with different symbols indicating different final states reached from small amplitude perturbations (see text). The solution profiles at locations (a)–(f) straddling the fold at γ_3^{DMS} are shown in Fig. 19. (b) Space–time plot of $V(x, t)$ showing the fast transition from the localized state (i) on the upper branch to the corresponding state on the lower branch.
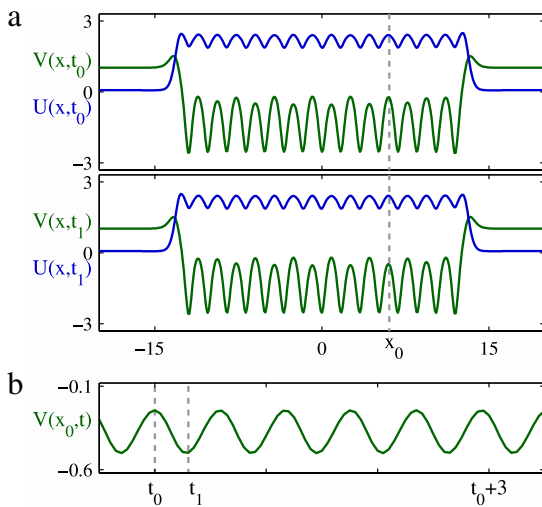

Fig. 24. (a) Snapshots of the solution profile at two instants half an oscillation period apart ($t_1 - t_0 \approx 0.3$), corresponding to maxima of the oscillation amplitude. (b) The time series $V(x_0, t)$ at fixed $x_0 \approx 6.05$.

above the saddle–node at γ_3^{DMS} and a lower part below it. In this interval the localized states on the upper branch evolve rapidly into those on the lower branch (e.g., Fig. 23(b)). Consequently, in the following we focus only on the time evolution of localized states on the lower branch. For these states we find that the fronts remain pinned when $\gamma_C < \gamma < \gamma_2^{DMS}$ (circles) but depin and move inward when $\gamma_3^{DMS} < \gamma < \gamma_C$ (upward-pointing triangles). Simulations show that in the former case the localized state is either time-independent and stable ($\gamma_B < \gamma < \gamma_2^{DMS}$, filled circles) or that it oscillates in time ($\gamma_C < \gamma < \gamma_B$, unfilled circles). An example of such an oscillatory localized structure is shown in Fig. 24. This oscillatory state, which may have arbitrarily large spatial extent, will be called an extended breather and resembles breathers identified in other forced dissipative systems [36]. In the case $\gamma_3^{DMS} < \gamma < \gamma_C$ both the inner wave train and the fronts are unstable to oscillations and these oscillations lead to depinning and ultimate collapse of the structure (unfilled triangles, e.g., Fig. 25). This collapsing state, with occasional interludes of meta-stability, will be called a Hanoi tower.

We note that the pinning region, $\gamma_C < \gamma < \gamma_2^{DMS}$, is narrower than the snaking region containing the localized states. A similar reduction in the interval of stable localized states is observed in the Swift–Hohenberg equation when two-dimensional perturbations of localized stripes are admitted [1]. The reason is simple:
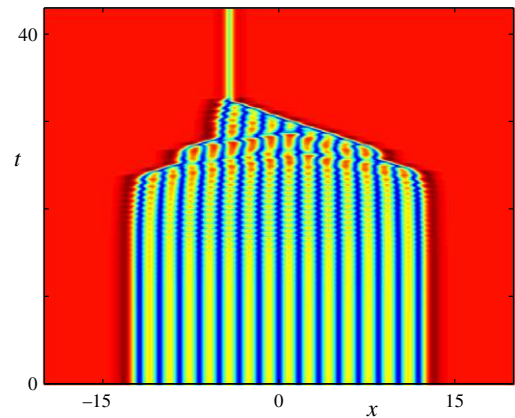

Fig. 25. Space–time plot showing the evolution of $V(x, t)$ corresponding to the localized state (iii) in Fig. 23(a) into a Hanoi tower. The final state is a stable spot.

depending on parameters the two-dimensional perturbations may lead to the depinning of the fronts that would otherwise remain pinned, just as here the temporal oscillation of the fronts also leads to depinning. In both cases the result is a reduced interval of parameter values in which the fronts remain pinned, and hence a reduced parameter interval containing stable spatially localized states.

5.2.1. Extended breather

As already mentioned, localized states like (ii) in Fig. 23(a) are subject to an oscillatory instability, which is absent from variational systems. In this case, the only linearly unstable modes are a pair of odd parity Hopf modes $A_H(x)$ and $\bar{A}_H(x)$ with growth rates $\sigma \pm i\omega$ ($\sigma > 0, \omega > 0$). The amplitude of these modes peaks in the center of the localized state and decreases towards the fronts on either side indicating that the oscillatory mode is a body mode. Decaying oscillations of this type are also visible in Fig. 23(b), between $t \approx 2$ and $t \approx 5$. Fig. 24(a) shows the solution profiles at maximum amplitude, half an oscillation period apart, once the oscillation is fully developed. As expected, the profiles are related to one other by the spatial reflection $x \rightarrow -x$.

5.2.2. Hanoi tower

As shown in Fig. 25, localized states like (iii) in Fig. 23(a) are subject to both oscillatory and depinning instabilities. The linearly unstable modes with the largest growth rates come in several complex conjugate pairs. The most unstable mode is the odd parity Hopf mode already encountered in the extended breather. The

second and third most unstable modes are also body modes, this time an even parity Hopf mode and a second odd parity Hopf mode. The fourth most unstable mode is an oscillatory wall mode with support around the fronts. This pair may be either even or odd, and is directly responsible for the collapse of the structure shown in Fig. 25, i.e., this is the mode that is responsible for the depinning of the fronts.

The presence of multiple instabilities often leads to complicated temporal dynamics. Indeed, we find that the shape of the Hanoi tower depends sensitively on γ as well as on the initial condition. An example can be seen in Fig. 25, where small amplitude but asymmetric noise in the initial condition is amplified by the growing instability leading to a considerable displacement of the final stable pulse from the center at $x = 0$.

6. Conclusion

In this paper we have identified a new mechanism for the growth of spatially localized structures as these structures are followed in parameter space. In contrast to the behavior familiar from existing studies of the Swift–Hohenberg equation and of localized states in different types of convection in which the structures grow by nucleating new cells at the location of the bounding fronts, the states we have found in the forced complex Ginzburg–Landau equation grow by the fission of the cell in the center of the structure, followed by outward displacement of all existing cells. We have called this mechanism defect-mediated snaking to contrast it with regular homoclinic snaking mentioned above, and think of the mechanism as a steady-state analog of the familiar target in which a wave is emitted from a central pacemaker symmetrically in both directions.

We have found DMS in the FCGLE with both 2:1 and 1:1 resonance. In the 2:1 case this mechanism appears to be present only in the self-exciting case and hence the localized states created by this mechanism are unstable. However, owing to the "reciprocity" between localized states asymptotic to a homogeneous background state and holes in a periodic state [37,31] we conjecture that stable reciprocal versions of these states may also be present in the DMS region. In an attempt to find stable localized states with defects in the center we turned to the 1:1 resonance. We have identified a DMS region in this equation also, but the requisite defect states were found to remain unstable although they now connect stable, defect-free portions of the branch (Fig. 15).

We have observed differences in the motion of the bounding fronts outside the pinning region as well. In the regular scenario the fronts depin above the pinning region and propagate outwards as a result of sequential nucleation of cells at the location of the fronts. Thus the passage of the front replaces the homogeneous state by a cellular state, but no motion of existing cells takes place. In contrast, in the 1:1 resonance case we have seen a different mechanism. The fronts still drift outwards with a speed proportional to the square root of the distance from the upper boundary of the DMS region, as in the regular case, but this time no nucleation of new cells at the location of the fronts takes place. Instead, the bounding cells are continually pushed outwards as phase slips repeatedly insert new roll pairs either symmetrically between the outer front and the center of the localized structure, or in the center. We have conjectured that these phase slips are triggered by the Eckhaus instability as the dilating structure is stretched by the moving fronts and its wavenumber pushed outside the Eckhaus-stable band. The reverse process occurs below the DMS region.

We leave a number of questions to future work. Among these we list the determination of the Eckhaus stability boundary for localized structures, the prediction of the speed of the fronts and the confirmation of its conjectured relation to the frequency of the observed phase slips. The transition from collapsed snaking to defect-mediated snaking remains incompletely understood. In addition, since the FCGLE reduces to the real Swift–Hohenberg equation in appropriate regimes [19] DMS may turn into regular homoclinic snaking as parameters are varied. How this might happen is also unclear.

Appendix. The supercritical Turing bifurcation

The Turing bifurcation at $\gamma = \gamma^T$ produces spatially periodic states with wavenumber k_T. Near this point we can write $\gamma = \gamma^T - \epsilon^2 \mu_2$, where $\epsilon \ll 1$ and $\mu_2 \sim O(1)$. With $A \equiv U + iV$, a multiscale expansion involving both the short spatial scale x and the long spatial scale $X = \epsilon x$ leads to

$$\begin{bmatrix} U \\ V \end{bmatrix} = \begin{bmatrix} U_0 \\ V_0 \end{bmatrix} + \epsilon \begin{bmatrix} \xi \\ 1 \end{bmatrix} \{ \mathcal{A} e^{ik_T x} + \bar{\mathcal{A}} e^{-ik_T x} \} + O(\epsilon^2).$$

Here the first term represents the equilibrium A^+. In the second term $\mathcal{A}$ is a complex function of X that satisfies the Ginzburg–Landau equation with real coefficients

$$\mathcal{A}_{XX} = -q_1 \mu_2 \mathcal{A} + q_2 |\mathcal{A}|^2 \mathcal{A} + O(\epsilon). \tag{20}$$

The coefficients in this equation are computed in Ref. [30] for the 2:1 resonance, and in Ref. [34] for the 1:1 resonance. These calculations show that $q_1 > 0$, $q_2 > 0$. Consequently the periodic states bifurcate supercritically, i.e., towards smaller γ ($\mu_2 > 0$).

The Turing bifurcation at $\gamma = \gamma^T$ corresponds to a reversible Hopf bifurcation with 1:1 resonance in space. Existing analysis of the corresponding normal form sheds light on the origin of homoclinic orbits to periodic wavetrains that are of interest here in connection with the defect states that play such a prominent role in defect-mediated snaking. The normal form for this bifurcation is [28]

$$\begin{aligned} A' &= ik_T A + B + iAP(\mu; y, w), \\ B' &= ik_T B + iBP(\mu; y, w) + AQ(\mu; y, w), \end{aligned} \tag{21}$$

where $y \equiv |A|^2$, $w \equiv \frac{i}{2}(A\bar{B} - \bar{A}B)$, the overbar refers to complex conjugation, and in the context of spatial dynamics the prime denotes differentiation with respect to x; μ is an unfolding parameter analogous to $\gamma^T - \gamma$. The functions A and B transform under spatial reflection as $(A, B) \rightarrow (\bar{A}, -\bar{B})$, and P and Q are polynomials with real coefficients:

$$\begin{aligned} P(\mu; y, w) &= p_1 \mu + p_2 y + p_3 w + \cdots, \\ Q(\mu; y, w) &= -q_1 \mu + q_2 y + q_3 w + \cdots. \end{aligned} \tag{22}$$

The 1:1 Hopf bifurcation from the trivial state $A = B = 0$ occurs at $\mu = 0$; by convention $q_1 > 0$ so that this state is hyperbolic in the region $\mu < 0$ and elliptic in $\mu > 0$. As shown in [28] the normal form (21) is an integrable two degree of freedom Hamiltonian system. This is true regardless of the system from which it is derived, and in particular it applies to systems that are not variational in time or Hamiltonian in space. Analysis shows that small amplitude orbits homoclinic to the trivial state are present for $\mu < 0$, $|\mu| \ll 1$, provided $q_2 < 0$ (the subcritical case). Here we consider the case $q_2 > 0$ (the supercritical case).

We write $(A, B) = (\epsilon \mathcal{A}(X), \epsilon^2 \mathcal{B}(X)) e^{ik_T x}$, where $X \equiv \epsilon x$, and write $\mu = \epsilon^2 \mu_2$. Thus P and Q in Eq. (22) become

$$\begin{aligned} P &= \epsilon^2 (p_1 \mu_2 + p_2 |\mathcal{A}|^2) + O(\epsilon^3), \\ Q &= \epsilon^2 (-q_1 \mu_2 + q_2 |\mathcal{A}|^2) + O(\epsilon^3). \end{aligned} \tag{23}$$
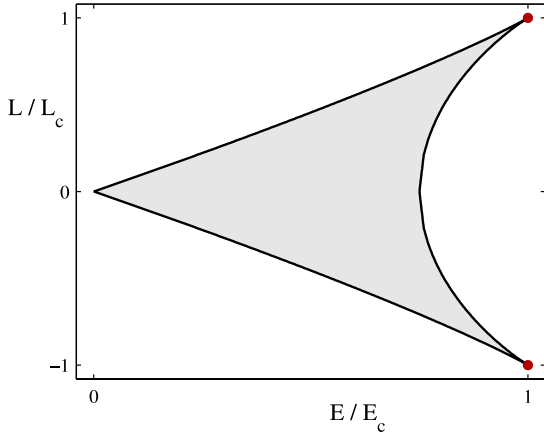
Fig. 26. Condition (36) in the $(E/E_c, L/L_c)$ plane. The red dots indicate the Eckhaus points. Quasiperiodic solutions exist in the shaded region, consistent with [28].

It follows from Eq. (21)(a) that $\mathcal{B} = \mathcal{A}' + O(\epsilon)$ and hence that Eq. (21)(b) reduces to Eq. (20).

Eq. (20) has the constant solution $|\mathcal{A}|^2 = q_1\mu_2/q_2 > 0$ corresponding to a Turing state with wavenumber k_T. The equation also possesses a front solution connecting two out-of-phase states with wavenumber k_T. To find this solution we write $\mathcal{A}(X) = R(X) \exp i\phi$, where ϕ is a constant, and integrate Eq. (20) once, obtaining

$$\frac{1}{2}R'^2 + V_0(R) = E. \tag{24}$$

Here $V_0 = \frac{1}{2}q_1\mu_2 R^2 - \frac{1}{4}q_2 R^4$ and E is a constant of integration. The front corresponds to a heteroclinic orbit between $\mathcal{A} = \pm R_0 \exp i\phi$, where $R_0^2 \equiv q_1\mu_2/q_2 > 0$ and is present when $E = \frac{1}{4}\frac{q_1^2\mu_2^2}{q_2}$. Thus $R(X)$ satisfies

$$\frac{1}{2}R'^2 = \frac{1}{4}q_2(R_0^2 - R^2)^2 \tag{25}$$

and hence

$$R(X) = R_0 \tanh\left(\sqrt{\frac{q_1\mu_2}{2}}X\right). \tag{26}$$

This solution asymptotes to the uniform wavetrains $\pm R_0$ as $|X| \to \infty$, i.e., it describes a π change in the *spatial* phase of the wavetrain between $X = -\infty$ and $X = \infty$.

We now suppose that the spatial phase ϕ is not constant. In this case Eq. (24) becomes

$$\frac{1}{2}R'^2 + V_L(R) = E, \tag{27}$$

where

$$V_L \equiv \frac{1}{2}q_1\mu_2 R^2 - \frac{1}{4}q_2 R^4 + \frac{L^2}{2R^2} \tag{28}$$

and $R^2\phi' = L$. The solutions are thus specified by the two constants E and L, hereafter the energy and angular momentum, respectively.

In this case we define R_+ as the (larger) solution of $q_2 R^6 - q_1\mu_2 R^4 + L^2 = 0$ and choose $E = q_1\mu_2 R_+^2 - \frac{3}{4}q_2 R_+^4$. In this case $R(X)$ satisfies the equation

$$\frac{1}{2}R'^2 = \frac{q_2}{4R^2}(R_+^2 - R^2)^2[R^2 - 2(R_0^2 - R_+^2)], \tag{29}$$

where $R_0^2 - R_+^2 > 0$. This equation can also be solved in closed form:

$$R^2 = 2(R_0^2 - R_+^2) + (3R_+^2 - 2R_0^2)\tanh^2 \sqrt{\frac{q_2}{2}(3R_+^2 - 2R_0^2)}X. \tag{30}$$

As $|X| \to \infty$ this solution approaches R_+^2. We think of $\phi_X \equiv k(X)$ as the (local) wavenumber of the solution. Thus $k(X) \to L/R_+^2$ as $|X| \to \infty$.

In addition to the homoclinic connection to periodic states with the wavenumber L/R_+^2, there are also solutions in the form of constant amplitude wavetrains. For these solutions k is a constant, $k = k_\pm$, and the amplitude satisfies

$$R^2 = R_0^2 - \frac{k_\pm^2}{q_2} \equiv R_\pm^2. \tag{31}$$

Since for these solutions $k_\pm = L/R_\pm^2$ it follows that $L^2 = q_2 R_\pm^4(R_0^2 - R_\pm^2)$. Thus $R_0^2 > R_\pm^2$ and moreover $R_0^2(R_+^2 + R_-^2) = R_+^4 + R_+^2 R_-^2 + R_-^4$. It follows that the two roots degenerate into the same root $R_+^2 = R_-^2 \equiv R_c^2$, where

$$R_c^2 = \frac{2}{3}R_0^2. \tag{32}$$

This occurs at a critical value of the constants E and L given by

$$E_c = \frac{1}{3}q_2 R_0^4, \qquad L_c^2 = \frac{4}{27}q_2 R_0^6 \tag{33}$$

and corresponds to a critical wavenumber k_c given by

$$k_c^2 = \frac{1}{3}q_2 R_0^2. \tag{34}$$

The value $L = L_c$ represents the maximum permitted value of L. At this value the potential $V_L(R)$ has an inflection point; for $L > L_c$ the potential is a monotonic function of R and there are no equilibria or bound orbits.

We now examine the connection between the above analysis which follows closely Ref. [28] and the standard discussion of the Eckhaus or modulational instability. In the classical picture of this instability [35] we look for solutions of

$$\mathcal{A}_t = q_1\mu_2\mathcal{A} - q_2|\mathcal{A}|^2\mathcal{A} + \mathcal{A}_{XX} \tag{35}$$

of the form $\mathcal{A} = R \exp ikX$. Steady solutions of this form satisfy $R^2 = R_0^2 - \frac{k^2}{q_2}$. These states are marginally unstable with respect to long wavelength perturbations along the line $R_0^2 = \frac{3k^2}{q_2}$ within the existence region $k^2 \le q_2 R_0^2$. This line is the threshold for the Eckhaus instability which occurs in the region $\frac{1}{3}q_2 R_0^2 \le k^2 \le q_2 R_0^2$. Thus the amplitude of the wavetrain that becomes Eckhaus unstable is given by $R^2 = \frac{2}{3}R_0^2$ and its wavenumber is given by $k^2 = \frac{1}{3}q_2 R_0^2$, i.e., the classical Eckhaus instability corresponds precisely to the point $(E, L) = (E_c, L_c)$, as noted already by Iooss and Pérouème [28]. In other words, the classical Eckhaus instability corresponds to the formation of a *degenerate homoclinic orbit* within the spatial dynamics approach. However, the spatial dynamics approach predicts a variety of additional quasiperiodic states corresponding to nonlinear oscillations about $R = R_-$. These can be written down explicitly in terms of elliptic functions and exist for $E_-(L) < E \le E_+(L)$, where $E_\pm(L)$ are the two roots of the equation

$$x(4x^2 - 3x - 6y) + y(y + 4) = 0 \tag{36}$$

and $x \equiv E/E_c < 1$, $y \equiv L^2/L_c^2 < 1$. Thus

$$y = 3x - 2 \pm 2(1 - x)^{3/2}. \tag{37}$$

These conditions define the region computed in Ref. [28] (Fig. 26). We do not compute these states explicitly except to note that both the amplitude and wavenumber of these states oscillate periodically in space.

Some of the solutions discussed in this Appendix are also encountered in Section 7 of [38].

References

[1] J. Burke, E. Knobloch, Homoclinic snaking: structure and stability, Chaos 17 (2007) 037102-1–037102-15.
[2] A.R. Champneys, Homoclinic orbits in reversible systems and their applications in mechanics, fluids and optics, Physica D 112 (1998) 158–186.
[3] O. Batiste, E. Knobloch, A. Alonso, I. Mercader, Spatially localized binary-fluid convection, J. Fluid Mech. 560 (2006) 149–158.
[4] A. Bergeon, E. Knobloch, Spatially localized states in natural doubly diffusive convection, Phys. Fluids 20 (2008) 034102-1–034102-8.
[5] Y. Pomeau, Front motion, metastability and subcritical bifurcations in hydrodynamics, Physica D 23 (1986) 3–11.
[6] J. Burke, E. Knobloch, Localized states in the generalized Swift–Hohenberg equation, Phys. Rev. E 73 (2006) 056211-1–056211-15.
[7] J. Burke, E. Knobloch, Snakes and ladders: localized states in the Swift–Hohenberg equation, Phys. Lett. A 360 (2007) 681–688.
[8] P.D. Woods, A.R. Champneys, Heteroclinic tangles and homoclinic snaking in the unfolding of a degenerate reversible Hamiltonian–Hopf bifurcation, Physica D 129 (1999) 147–170.
[9] J. Burke, E. Knobloch, Multipulse states in the Swift–Hohenberg equation, in: Xiaojie Hou, Xin Lu, Alain Miranville, Jianzhong Su, Jianping Zhu (Eds.), Dynamical Systems and Differential Equations, in: Discrete and Continuous Dynamical Systems—Suppl., 2009, pp. 109–117.
[10] M. Beck, J. Knobloch, D.J.B. Lloyd, B. Sandstede, T. Wagenknecht, Snakes, ladders, and isolas of localised patterns, SIAM J. Math. Anal. 41 (2009) 936–972.
[11] J. Burke, J.H.P. Dawes (in preparation).
[12] A. Bergeon, E. Knobloch, Periodic and localized states in natural doubly diffusive convection, Physica D 237 (2008) 1139–1150.
[13] P. Coullet, K. Emilsson, Strong resonances of spatially distributed oscillators: a laboratory to study patterns and defects, Physica D 61 (1992) 119–131.
[14] C. Elphick, G. Iooss, E. Tirapegui, Normal form reduction for time-periodically driven differential equations, Phys. Lett. A 120 (1987) 459–463.
[15] H. Arbell, J. Fineberg, Temporally harmonic oscillons in Newtonian fluids, Phys. Rev. Lett. 85 (2000) 756–759.
[16] O. Lioubashevski, Y. Hamiel, A. Agnon, Z. Reches, J. Fineberg, Oscillons and propagating solitary waves in a vertically vibrated colloidal suspension, Phys. Rev. Lett. 83 (1999) 3190–3193.
[17] S. Longhi, Spatial solitary waves in nondegenerate optical parametric oscillators near an inverted bifurcation, Opt. Commun. 149 (1998) 335–340.
[18] P.B. Umbanhowar, F. Melo, H.L. Swinney, Localized excitations in a vertically vibrated granular layer, Nature 382 (1996) 793–796.
[19] D. Blair, I.S. Aranson, G.W. Crabtree, V. Vinokur, L.S. Tsimring, C. Josserand, Patterns in thin vibrated granular layers: interfaces, hexagons, and superoscillons, Phys. Rev. E 61 (2000) 5600–5610.
[20] V. Petrov, Q. Ouyang, H.L. Swinney, Resonant pattern formation in a chemical system, Nature 388 (1997) 655–657.
[21] A. Yochelis, J. Burke, E. Knobloch, Reciprocal oscillons and nonmonotonic fronts in forced nonequilibrium systems, Phys. Rev. Lett. 97 (2006) 254501-1–254501-4.
[22] D. Gomila, A.J. Scroggie, W. Firth, Bifurcation structure of dissipative solitons, Physica D 227 (2007) 70–77.
[23] V.B. Taranenko, K. Staliunas, C.O. Weiss, Spatial soliton laser: localized structures in a laser with a saturable absorber in a self-imaging resonator, Phys. Rev. A 56 (1997) 1582–1591.
[24] V.B. Taranenko, K. Staliunas, C.O. Weiss, Pattern formation and localized structures in degenerate optical parametric mixing, Phys. Rev. Lett. 81 (1998) 2236–2239.
[25] E.J. Doedel, B. Oldeman, AUTO07p: continuation and bifurcation software for ordinary differential equations, Technical Report, Concordia University, 2009.
[26] L.A. Belyakov, Bifurcation of systems with homoclinic curve of a saddle-focus with saddle quantity zero, Mat. Zametki 36 (1984) 838–843.
[27] R.L. Devaney, Homoclinic orbits in Hamiltonian systems, J. Differential Equations 21 (1976) 431–438.
[28] G. Iooss, M.C. Pérouème, Perturbed homoclinic solutions in reversible 1:1 resonance vector fields, J. Differential Equations 102 (1993) 62–88.
[29] A. Bergeon, J. Burke, E. Knobloch, I. Mercader, Eckhaus instability and homoclinic snaking, Phys. Rev. E 78 (2008) 046201-1–046201-16.
[30] J. Burke, A. Yochelis, E. Knobloch, Classification of spatially localized oscillations in periodically forced dissipative systems, SIAM J. Appl. Dyn. Syst. 7 (2008) 651–711.
[31] E. Knobloch, Spatially localized structures in dissipative systems: open problems, Nonlinearity 21 (2008) T45–T60.
[32] J. Knobloch, T. Wagenknecht, Homoclinic snaking near a heteroclinic cycle in reversible systems, Physica D 206 (2005) 82–93.
[33] D. Avitabile, D.J.B. Lloyd, J. Burke, E. Knobloch, B. Sandstede, To snake or not to snake in the planar Swift–Hohenberg equation, SIAM J. Appl. Dyn. Syst. 9 (2010) 704–733.
[34] Y.-P. Ma, E. Knobloch, Localized states in the forced complex Ginzburg–Landau equation with 1:1 resonance, Preprint, 2010.
[35] R. Hoyle, Pattern Formation, Cambridge University Press, Cambridge, 2006.
[36] R.J. Deissler, H.R. Brand, Periodic, quasiperiodic and chaotic localized solutions of the quintic complex Ginzburg–Landau equation, Phys. Rev. Lett. 72 (1994) 478–481.
[37] P. Coullet, C. Riera, C. Tresser, A new approach to data storage using localized structures, Chaos 14 (2004) 193–198.
[38] B. Sandstede, A. Scheel, Defects in oscillatory media: toward a classification, SIAM J. Appl. Dyn. Syst. 3 (2004) 1–68.